Investigation on Ammonium Perchlorate Based Electrically Controlled Propellants

Nicholas P. Fiorenza

Thesis submitted to the Faculty of the
Virginia Polytechnic Institute and State University
in partial fulfillment of the requirements for the degree of

Master of Science
in
Aerospace Engineering

Gregory Young, Chair
Joseph A. Schetz
Joseph Meadows

May 8, 2025
Blacksburg, Virginia

Keywords: Electrically Controlled Combustion, Polymer Electrolytes, Rocket Propulsion

Investigation on Ammonium Perchlorate Based Electrically Controlled Propellants

Nicholas P. Fiorenza

(ABSTRACT)

An experimental study exploring the ignition behavior of an electrically controlled gel monopropellant (ECGP) composed of an ionically conducting liquid polymer (polyethylene glycol) and ammonium perchlorate (AP) was conducted. Complexation of AP with PEG enabled ion transport when a voltage was applied resulting in ignition. Although the propellant was manufactures by solution casting, the final product contained no solvent as confirmed by thermogravimetric analysis. Several electrode configurations were explored which balanced or limited either oxidation or reduction at the electrodes. Other than when reduction was limited, ignition always occurred at the anode. Limiting reduction resulted in an apparent increase in the bulk resistivity of the propellant which was attributed to enhanced bubble/-gas formation at the cathode. The increase in apparent bulk resistivity resulted in enhanced joule heating and a shift in ignition mechanism from predominately electrochemical to thermal. This behavior is supported by analysis of the current data and infrared temperature measurements. The temperature measurements demonstrate that the highest temperatures occur where the processes are limited. The competition between thermally and electrolytically induced ignition and combustion characteristics of the gel polymer electrolyte will be presented in this thesis.

Investigation on Ammonium Perchlorate Based Electrically Controlled Propellants

Nicholas P. Fiorenza

(GENERAL AUDIENCE ABSTRACT)

There are two main classes of rockets: one that utilizes liquid propellants, and one that utilizes solid propellants. All liquid propellants are susceptible to leaks, and many traditional liquid propellants are both toxic and/or carcinogenic. As for solid propellants, their primary drawbacks are their inability to be throttled and their inability to be easily extinguished, or in other words, once they are lit there is little control. This research investigates an alternative approach in the development of an electrically controlled propellant where the decomposition mechanisms of a polyethylene glycol (PEG) based propellant is investigated. The polymer is incorporated as both a binder and a fuel source with ammonium perchlorate ionic salt as the primary oxidizer. Two different experimental configurations are studied with varying electrode geometries. Under an applied voltage, there are two competing and complementary decomposition mechanisms: thermal and electrochemical, which can be tailored by controlling the surface area of the electrodes to limit the electrochemistry occurring at one side.

Dedication

For my family and loved ones, whose support is unwavering and invaluable.

Acknowledgments

First, thank you to my advisor Dr. Greg Young whose mentorship and guidance over the last few years has been vital to the completion of this research. In addition, this work would not have been possible without advice and support from colleagues and peers, in particular, Sean Whalen, Dale LeFebvre, Nick Keddy, and Grace Hadley. Thank you as well to my advisors Dr. Joseph Schetz and Dr. Joseph Meadows. This work was made possible by the use of Virginia Tech's Materials Characterization Facility, which is supported by the Institute of Critical Technology and Applied Science, the Macromolecules Innovation Institute, and the Office of the Vice President for Research and Innovation. The research presented here would not have been possible without the funding from the Office of Naval Research and Program Officer Dr. Chad Stoltz under Grant No. N00014-23-1-2430.

Contents

List of Figures

List of Tables

List of Abbreviations

$\dot{m}$	Mass Flow Rate
$\dot{r}$	Propellant Regression Rate
Λ	Molar Conductivity
μ	Ion Mobility
$\nabla\phi(\vec{r})$	Electric Potential Gradient
ρI_{sp}	Density-Specific Impulse
ρ	Charge Density
$\mathcal{T}$	Thrust
$\vec{r}$	Position Vector
A_e	Nozzle Exit Area
D	Diffusion Coefficient
E	Electric Field
F	Faraday Constant
g_e	Gravitational Acceleration
I_{sp}	Specific Impulse
k_B	Boltzmann Constant

p_a	Atmospheric Pressure
p_c	Chamber Pressure
p_e	Nozzle Exit Pressure
r	Hydrodynamic Radius
R_u	Universal Gas Constant
T	Temperature
u	Ion Drift Velocity
u_e	Nozzle Exit Velocity
u_{eq}	Equivalent Exhaust Velocity
V	Voltage
z	Ionic Charge
AFRL	Air Force Research Laboratory
AN	Ammonium Nitrate
AP	Ammonium Perchlorate
ATR	Attenuated Total Reflectance
CEA	Chemical Equilibrium with Applications
DC	Direct Current
DSC	Differential Scanning Calorimetry
ECGP	Electrically Controlled Gel Propellant

ECP	Electrically Controlled Propellant
ECSP	Electrically Controlled Solid Propellant
EG	Ethylene Glycol
FTIR	Fourier Transform Infrared Spectroscopy
GPE	Gel Polymer Electrolyte
HAN	Hydroxyl Ammonium Nitrate
HMX	Tetrahexamine Tetranitramine
LP	Lithium Perchlorate
MWCNT	Multi-walled Carbon Nanotube
NTO	Nitrogen Tetroxide
PE	Polymer Electrolyte
PEG	Polyethylene Glycol
PEO	Polyethylene Oxide
PMMA	Poly-methyl Methacrylate
PVA	Polyvinyl Alcohol
SPE	Solid Polymer Electrolyte
SRM	Solid Rocket Motor
TGA	Thermogravimetric Analysis

Chapter 1

Introduction

Rocket propulsion systems are distinct from air-breathing propulsion systems in that they carry the required fuel and oxidizer onboard. This distinction leads to several advantages, including operation in space environments, higher thrust to weight ratios, and a thrust profile largely independent from flight conditions. By utilizing an oxidizer that is more concentrated than atmospheric air, higher combustion temperatures can also be achieved. This thermal energy is converted into kinetic energy through a nozzle, and the amount of kinetic energy that can be produced is directly related to the heat produced through the combustion of the propellant. Rocket motors are typically ignited through an igniter wire, or a spark, potentially in a preburner before the main thrust chamber [1]. An alternative being explored is in electrically controlled propellants, which are responsive and able to be controlled through electrical stimuli. The research detailed in this thesis focuses on the exploration of ignition properties of a gel monopropellant characterized by the use of a gel polymer electrolyte, which is decomposed and ignited through electrochemical means. This chapter briefly covers a categorization of rocket propulsion systems and their respective historical development and the fundamentals of rocket propulsion, to provide a background and motivation for the research conducted in this thesis.

1.1 Propulsion System Classifications

Jet propulsion typically refers to the motion of a body as a result of the reactionary force to the momentum of an ejected mass, and this can be classified as either a rocket or duct propulsion system [1]. Rocket propulsion systems expel a stored propellant to produce momentum, whereas duct propulsion includes air-breathing engines. Duct propulsion produces momentum through the combustion of stored onboard fuel with atmospheric air and can be categorized by those containing turbomachinery, eg, (turbofans and turbojets), and those without turbomachinery, eg, (ramjets and scramjets) [1, 2].

1.2 Rocket Propulsion Systems

Rocket propulsion has several advantages over air-breathing systems. This includes a high thrust-to-weight ratio, operation in space, or oxygen-poor environments, and a thrust profile that is relatively independent of flight conditions [1]. A fundamental metric of rocket performance metrics in the specific impulse (I_{sp}), which is a parameter derived from the rocket thrust equation, shown in Equation 1.1 [2].

$$\mathcal{T} = \dot{m}u_e + (p_e - p_a)A_e \tag{1.1}$$

where $\mathcal{T}$ is the thrust, $\dot{m}$ is the mass flow rate of propellant from the rocket, u_e is the exit velocity of the gas exiting the nozzle, p_e is the pressure at the exit plane of the nozzle, p_a is the atmospheric pressure, and A_e is the area of the exit plane of the nozzle. Equivalent exhaust velocity, u_{eq}, is defined in Equation 1.2, which allows us to write the specific impulse of the vehicle as seen in Equation 1.3, where g_e is the acceleration due to gravity [3].

$$u_{eq} = \frac{\mathcal{T}}{\dot{m}} = u_e + \frac{(p_e - p_a)}{\dot{m}} A_e \tag{1.2}$$

$$I_{sp} = \frac{u_{eq}}{g_e} \tag{1.3}$$

Specific impulse (I_{sp}) is a representation of thrust produced per unit weight flow of the propellant. It is measured in seconds, and a larger value indicates that less propellant is expelled to create an equivalent thrust on a mass basis [2]. Density-specific impulse (ρI_{sp}) evaluates the same metric on a per volume basis. A higher density propellant enables a smaller space allocation for the propellant, leading to a smaller overall vehicle, or more propellant mass can be stored in the same volume. The ideal rocket equation (Equation 1.4) further demonstrates the importance of propellant density and specific impulse in rocket performance. In Equation 1.4, m_o is the initial rocket mass, V_p is the volume of the propellant, and ρ_p is the propellant density.

$$\Delta \nu = I_{sp} g_e \ln\left(\frac{m_o}{m_o - \rho_p V_p}\right) \tag{1.4}$$

Here, the denominator $(m_o - \rho_p V_p)$ can be rewritten as m_f or the final mass of the rocket because $\rho_p V_p$ represents the mass of propellant burned. The total velocity change of the rocket (Δv) is directly related to the amount of propellant mass in the vehicle and the specific impulse, depicted in Fig. 1.4. Thus, increasing propellant density allows for a larger mass to be stored in the same volume, and the Δv increases.

Another pertinent propellant performance parameter is the characteristic exhaust velocity (c^*), which is useful in comparing combustion performance between propulsion systems and propellants, independent of nozzle geometry as defined in Equation 1.5.

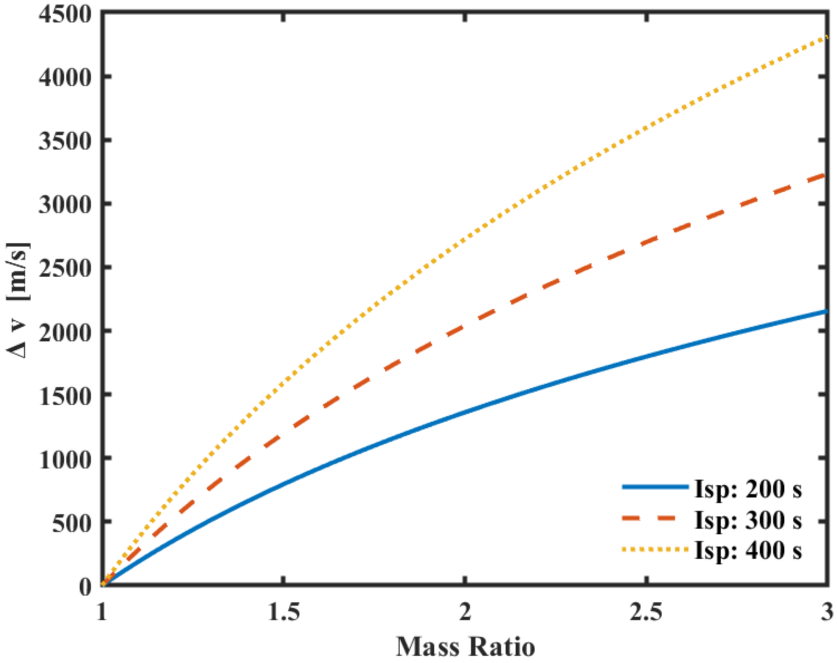

Figure 1.1: Δ V for a given I_{sp} and mass ratio

$$c^* = \frac{p_c A^*}{\dot{m}} \tag{1.5}$$

Where A^* is the nozzle throat area, and p_c is the chamber pressure.

1.2.1 Historical Development of Rocket Propulsion

The oldest form of jet propulsion dates back to Chinese gunpowder used to propel fireworks in the twelfth century, which was formulated from sulfur, charcoal dust, and a naturally occurring potassium nitrate called saltpeter [4]. Over the following centuries, many civilizations developed forms of gunpowder and solid rockets in the form of missiles for use in combat by the eighteenth and nineteenth centuries [2]. In the early 19th century, a British colonel by the name of William Congreve performed experiments and developed what is now known as the Congreve rocket. The Congreve rocket was a development on Indian rockets of the time and utilized an iron case packed with black powder. These rockets were used extensively in combat in the 19th century, as caliber classes were formed for use in a variety of applications, and range eventually climbed to over a kilometer [4]. Modern development of solid propellants began with Dr. Theodore von Karman at the Guggenheim Aeronautical Laboratory (GALCIT) at the California Institute of Technology in the 1930s. Here he experimented with rocket motors utilizing gunpowder and an asphalt fuel binder mixed with a potassium perchlorate oxidizer [3]. During World War II, von Karman's group received funding to develop a jet-assisted-take-off (JATO) motor and moved off campus to become the Aerojet Engineering Corporation [3]. Aerojet quickly revolutionized solid rocket motors by introducing case-bonded motors, which led to double-base bonded propellants. This was generally an improvement over propellants prepared in a cartridge and then inserted into the motor case [3]. Initial asphalt binders suffered from poor performance, and thus, synthetic polymers were introduced as binders in solid propellants. Initial research turned to polybutadiene-styrene and polychloroprene as binders, however, a castable polysulfide binder from Thiokol was the most promising [3]. The oxidizer used in solid rocket propellants was primarily potassium perchlorate up until the late 1940s when ammonium perchlorate was introduced to increase performance when Thiokol went on to produce polysulfide and ammonium perchlorate based rocket propellants for the United States military [5, 6]. Performance increasing additives, specifically aluminum and energy-dense compounds, such as tetrahexamine tetranitramine (HMX), were implemented in the 1950s and 1960s, and as such, specific impulses around 250s were achievable [3, 6]. At the same time, Thiokol continued research in developing polymers for solid rockets and introduced hydroxyl- and carboxyl- terminated polybutadiene [5].

Liquid rockets have a shorter history, as they were first proposed by Konstantin Tsiolkovsky in 1903 when he published an article titled *Exploration of Space with Reactive Devices*, in which he recognized that solid gunpowder would not be energetic enough to propel a rocket out of the atmosphere. He proposed the use of liquid hydrogen as the fuel and liquid oxygen as the oxidizer [2, 7]. Tsiolkovsky conducted no experimentation, and his work received little attention; his derivation of the ideal rocket equation (Equation 1.4) went largely unattributed until his work was republished in Germany in the 1920s. The first successful experiments of a liquid rocket were carried out by Robert H. Goddard, who also proposed using liquid hydrogen and liquid oxygen [8]. He went on to conduct experiments while serving as a professor at Clark University, in the 1920s and 1930s, with the first successful liquid rocket taking flight in 1926 using a gasoline and liquid oxygen based propellant [7]. During the interwar period, Goddard continued to develop liquid rocket technologies and amassed many patents on propellant feed systems and combustion chambers, and he introduced gyroscopes for increased control and stability of rockets. At the same time, in Germany, Hermann Oberth was independently pioneering liquid rocket technology. Oberth used a combination of liquid hydrogen and various alcohols as fuels for his rockets, and in 1923 he published a book titled *The Rocket into Planetary Space* where he developed substantial theory on liquid rocket propulsion [2]. This included an independent derivation of the ideal rocket equation and the idea of multi-stage rockets to reduce excess mass after the initial launch to increase $\Delta\nu$ [9]. Contributions to early liquid rocket developments were achieved by V.P Glushko from Russia and Luigi Crocco from Italy, where in 1930 they separately became the first to utilize a liquid oxidizer other than oxygen in 1930 by using nitrogen tetroxide (NTO). Additionally, various fuels experimented with at this time included kerosene, methane, and ethyl alcohol, the latter of which was utilized in the V-2 rocket, developed in 1936 by a student of Oberth named Wernher von Braun [7].

Crocco also pioneered the development of monopropellants, which offered greater simplicity and reduced cost compared to conventional bipropellants developed at the time [7]. His funding for monopropellants ended in 1935; however, he experimented with methyl alcohol mixtures and nitroglycerin before moving onto nitromethane, which proved to be a promising alternative [10]. Helmuth Walter of the Chemical State Institute in Berlin was also a significant contributor to the development of early monopropellants, however, his work was kept private at the time by the Luftwaffe. Walter developed a monopropellant based on an 80% hydrogen peroxide solution, which decomposes into oxygen and superheated steam under proper heating. This monopropellant was utilized in the fuel supply subsystem of the aforementioned V-2 missile, where calcium permanganate was used as a catalyst [7]. The V-2 was critical to the further development of rockets, as the research became more readily available after the Second World War. In this era, the United States and the Soviet Union became influential players in the development of rocket engines and early space exploration.

The onset of the space race altered the primary motivation behind the development of liquid and solid rockets. In the United States, further development of propellants split into two distinct paths during the Cold War. The first was for use in orbital vehicles and strategic missiles. In this case, liquid hydrogen, kerosene, or alcohol were quickly decided upon as the best fuels, with liquid oxygen being the primary oxidizer. The Saturn V upper stage used liquid hydrogen fuel, the Sm-65 Atlas used kerosene, and the Mercury Redstone Rocket used ethyl alcohol, respectively. The second development path was into propellants with greater storage capabilities for use in tactical missiles. For these applications, hydrazine derivatives were cemented as the fuel of choice, with nitric acid or NTO as the primary oxidizing agent [7].

1.2.2 Solid Rocket Motors

A solid rocket propellant grain can be divided into two categories: a composite grain and a homogeneous/ double base grain. Composite solid propellants consist of a solid oxidizer and a fuel, typically micro- or nano-sized metal particles such as aluminum, mixed and suspended in a polymer binder. Homogeneous solid propellants are chemically linked, thus, the resulting structure is uniform throughout the propellant [11].

Figure 1.2 depicts a solid rocket motor (SRM) diagram. One primary advantage of an SRM is its simplicity, as there are few to zero mechanically complex parts. The SRM is composed of a propellant grain cast into a motor case, with an ignitor on one end and a nozzle on the other. Additionally, in modern applications, the propellant grain is typically bonded directly to the motor case, further reducing complexity. A secondary benefit of SRMs is in their storage and ease of handling. A solid propellant can be stable in long term storage for up to 30 years, and due to its solid nature, there is no risk for leakage or chemical spills [1]. In addition to being readily ignitable, there is minimal support equipment required to operate an SRM, allowing for relatively inexpensive maintenance and operation.

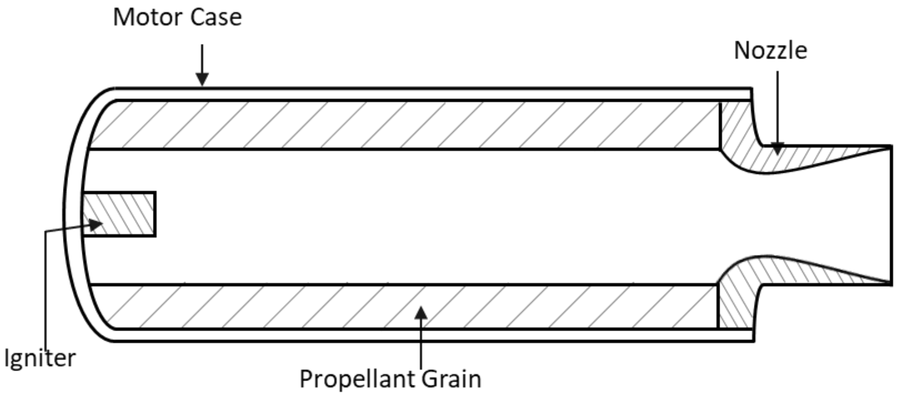

Figure 1.2: Simplified Solid Rocket Motor Schematic

SRM performance is governed by the rocket thrust equation described in Equation 1.1 where

$\dot{m}$, mass flow, is defined below in Equation 1.6. Here, $\dot{r}$ is the propellant linear burn rate, ρ_p is the propellant density, and A_b is the burning surface area of the propellant.

$$\dot{m} = \dot{r}\,\rho_p\,A_b \tag{1.6}$$

Further, the regression rate $\dot{r}$ can be defined by Saint-Robert's law (Equation 1.7) in which P_c is the combustor pressure and a and n are constants.

$$\dot{r} = a\,P_c^n \tag{1.7}$$

Lack of active control of a solid rocket is its biggest disadvantage. The propellant characteristics and grain and nozzle geometries are all set before ignition, yet these aspects have a primary role in the mass flow exiting the rocket. Chamber pressure can be controlled through a variable nozzle geometry or by off-gassing the combustor, however, the influence on propellant burn rate is secondary. Thrust profiles are determined by the evolution of the propellant grain geometry as the propellant regresses during combustion. Due to this, the thrust profile is determined by the initial propellant geometry. Various example geometries and their respective thrust profiles are shown in Fig. 1.3. Once ignited, the propellant will regress normal to the exposed surface, and the evolution of that surface is predetermined. The thrust generated can be influenced by the nozzle selection and initial temperature of the propellant, however, the profile can not be easily changed or manipulated once the motor is cast.

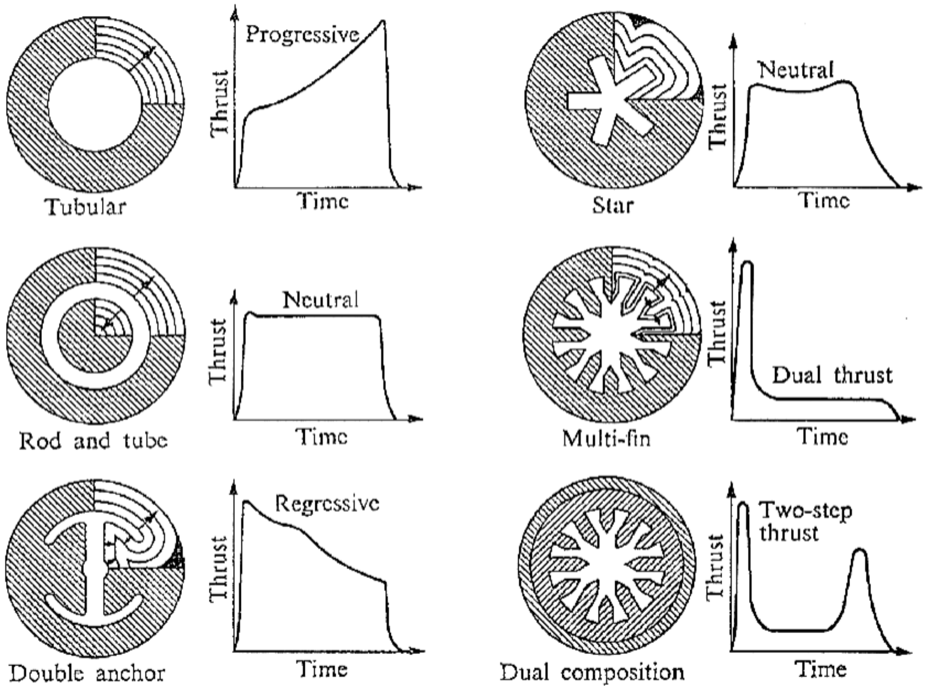

Figure 1.3: Thrust Profiles Across Propellant Grain Geometries [1]

1.2.3 Liquid Rocket Engines

Liquid rocket engines are generally classified by the propellant components with monopropellant systems and bi-propellant systems containing one and two components, respectively [1]. The classification can further be broken down into propellant feed type, application, staging, and other various factors. These classifications are helpful due to the difference in orbital-class rocket engines operating in a vastly different flight envelope than spacecraft propulsion systems. Orbital class engines typically use either a rocket-grade kerosene, liquid hydrogen, or liquid methane fuel with liquid oxygen as the oxidizer. These propellants generate a large specific impulse, which is crucial for space launches where the required Δv is large [7]. Satellite thrusters, on the other hand, typically use hypergolic propellants containing nitrogen tetroxide (NTO) and hydrazine to reduce complexity and cost by eliminating the need for an igniter. In this manner, the propellants decompose catalytically. [1, 2, 12].

Motors of this kind trade performance efficiency with both reductions in parasitic mass and complexity and long term storage capabilities [12].

Figure 1.4 depicts a pump fed, bi-propellant liquid rocket engine. In all liquid rocket engines, the propellant and oxidizer are stored outside of the combustion chamber, and in this case, are fed into the combustor through a turbine-driven pump. The alternative fuel feed method is a pressure fed propellant system, where the fuel and oxidizer tanks are pressurized, and the pressure differential between the storage tanks and the combustion chamber allows for the flow of propellant through the operation of valves in the system. In either case, the required flow rates of the oxidizer and fuel can be readily manipulated such that the thrust output can be throttled up or down on command by adjusting the flow rates. Additionally, the engine can also be shut down by stopping the flow of propellant and restarted again as desired. These propellant feed systems greatly increase the mechanical complexity of liquid-fueled rockets compared to a solid rocket motor, however, the throttling and restart capabilities are extremely useful in satellite control. A comprehensive list of advantages and disadvantages of solid and liquid propellants is found in Table 1.1.

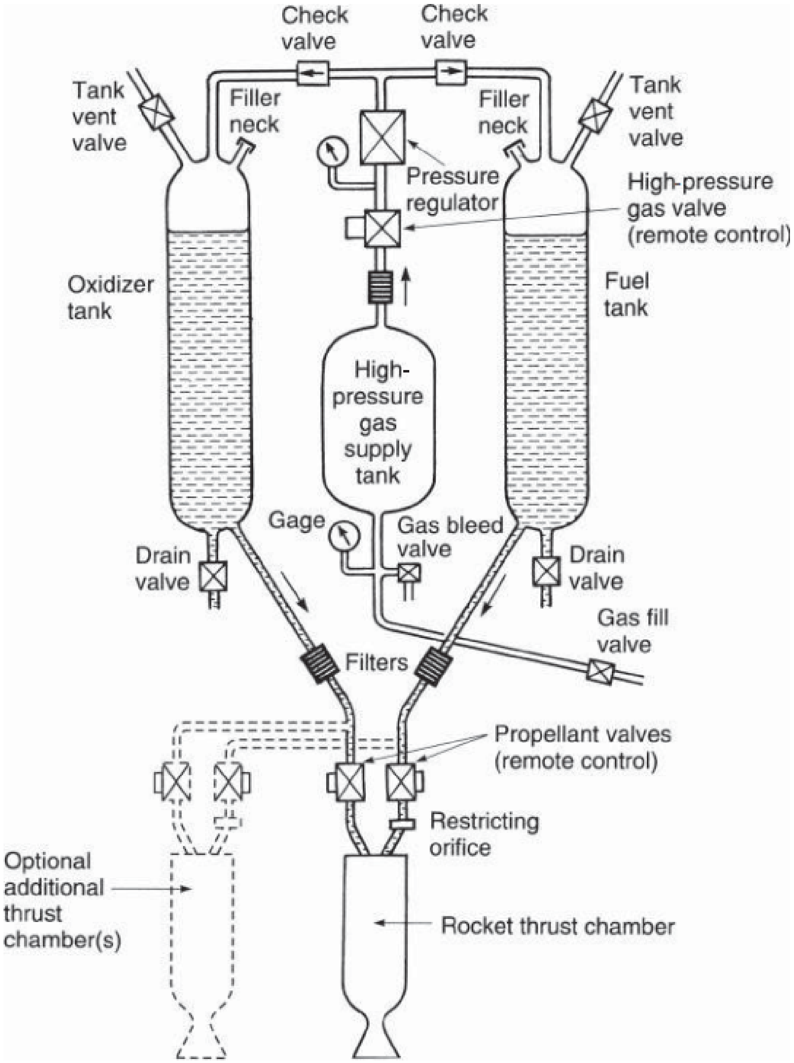

Figure 1.4: Pressure-fed Liquid Rocket Engine Schematic [1]

1.2.4 Gel Propellant Rockets

Gel propellants are an attempt to combine the benefits of both solid and liquid propellants. Conventionally, gel propellants are fed into a combustion chamber like a liquid, which enables a degree of throttling based on the rate at which the propellant is being fed. Gel propellants have low volatility and have storage capabilities similar to solid propellants, thus reducing the risk of spills or leakage [13, 14]. On the other hand, gels tend to suffer from combustion inefficiencies due to more complicated atomization and low combustion rates compared to conventional liquids [15]. Research on gel propellants typically investigates liquid fuels with added gelling agents to increase their viscosity and create a matrix for additives, including solid oxidizers and metals. Much like liquid propellants, gel propellants can be configured as bi-propellants or monopropellants. Bi-propellants utilize separate fuel and oxidizer components that are mixed into a solution, whereas a gel monopropellant is chemically linked with a premixed fuel and oxidizer. Theoretically, these propellant systems are safer to operate due to their decreased susceptibility to leakage [1].

Initial development of gel propellants was a derivation of solid propellants in which a propellant was immobile and cast into a motor case [16]. Modern gel propellants are shear-thinning, such that they are immobile with a high viscosity under no load, but will flow when a load is applied [16, 17]. Early experimentation by NASA in the 1960s incorporated liquid hydrogen gels in an attempt to increase propellant density while reducing complications due to liquid sloshing [18]. Much like solid propellants, micro- or nano-sized metal additives (typically aluminum) can be added to the gel to increase performance; however, in this case, consideration must be taken to ensure a homogeneous mixture and to avoid settling.

1.3 Spacecraft Monopellants

As mentioned previously, monopropellants are historically used extensively in spacecraft propulsion for attitude and control thrusters. Hydrazine and its derivatives have become the industry standard for spacecraft propellants since its first use in the Titan I upper stage in 1966 [19]. Hydrazine is easily stored, can be ignited hypergolically, demonstrates its versatility in being used as either a monopropellant or bipropellant, and at this point has

Table 1.1: Propellant Tradeoffs: Solid vs. Liquid

Solid Propellant	
Advantages	High energy density Long term storage capability No spill or leakage risk Easily ignited Design and operational simplicity
Disadvantages	Lack of throttling capabilities Often toxic exhaust products Total impulse/ Thrust profile unchangeable in flight Casting defects can lead to catastrophic failure Performance variation with temperature deviations Inadvertent ignition potential Inability to test before flight
Liquid Propellant	
Advantages	Throttling and restart capabilities Separation of fuel and oxidizer Ability to test before flight External control of thrust profile in flight Potential Reuseability
Disadvantages	Increased design complexity and vehicle mass Risk for spills and leakage Volumetrically less dense compared to solid propellants Cryogenic applications require further infrastructure and cost

established infrastructure and a history of success in space applications. [20].

Hydrazine as a monopropellant is typically decomposed through the Shell 405 catalyst, which contains an aluminum oxide and iridium activator. This catalytically decomposes the propellant on the order of milliseconds and produces an exothermic reaction yielding hydrogen, nitrogen, and ammonia gases as products [12]. Catalysts for monopropellant hydrazine can often be preheated such that the decomposition and ignition is near instantaneous, however, consideration must be made to material selection, as at elevated temperatures, hydrazine can be catalyzed by common materials [1, 12, 21]. As a bipropellant, hydrazine is commonly used as a fuel component with an NTO oxidizer, where the combination is hypergolic, which eliminates the need for an ignition system and increases both reliability and simplicity. Derivatives of hydrazine have also been introduced with the main goal of reducing the freezing point of hydrazine for greater applications in space environments. Two derivatives are unsymmetric dimethyl hydrazine (UDMH) and monomethyl hydrazine (MMH), which were developed to bring the freezing point from 275 K down to 216 K and 221 K, respectively [22]. These derivatives have a similar performance to hydrazine and are still hypergolic with NTO, which yields greater operability than hydrazine alone. Significant drawbacks of hydrazine are in toxicity and susceptibility to form explosive mixtures and become flammable in air, leading to spontaneous ignition [19, 23, 24].

1.3.1 Alternative to Hydrazine

The toxicity and carcinogenic nature of hydrazine have led to a search for alternatives, with the primary motivator being a non-toxic, green monopropellant [20, 23]. Defining ”green” in this case is a bit ambiguous, as there is no strict definition of what a green propellant is, however, the commonly accepted standards include a propellant with similar performance characteristics to hydrazine that demonstrates reduced toxicity and handling hazards associated with transportation [20, 23]. Many alternatives are categorized as energetic ionic liquids (EILs), however, various combinations of hydrogen peroxide and nitrous oxide alternatives are being considered [19, 20]. An ionic liquid refers to a premixed propellant in which an oxidizer salt has been dissolved into its cation-anion pairs and mixed into a fuel component.

These kinds of propellants have been implemented successfully in various configurations utilizing both hydroxyl ammonium nitrate (HAN) and ammonium dinitramide (ADN) as oxidizing agents [25, 26]. ADN was originally synthesized by Russian scientists in 1971, yet its discovery remained classified at the time, and the U.S separately synthesized ADN in 1988 [27]. In the early 1990s, ADN was the focus of a new high performance propellant by the Swedish Defense Research Agency, which resulted in the formulations of FLP-106 and LMP-103S [21, 23]. HAN based propellant research dates back to the 1970s by the U.S. Army in research for liquid propellant gun applications, which produced a propellant known as XM-46 [28]. This formulation suffered from sub-par performance, yet work done by the Air Force Research Lab (AFRL) in the 1990s yielded a higher performance HAN-based monopropellant, AF-M315E [29, 30, 31, 32]. In recent years, the Japan Aerospace Exploration Agency (JAXA) has implemented another HAN-based propellant, SHP-163 [33]. Modern EILs have outperformed hydrazine in many metrics, including specific impulse, and flame temperature [26, 29, 33]. Further, these blends do not possess the same level of toxicity risk and offer a lower flammability risk. Major drawbacks, however, are in their extreme oxidizer quantity, which impacts materials choices, and their poor storage nature due to evaporation [29]. Additionally, these propellants have demonstrated catalytic ignition and electrolytic decomposition due to their ionic nature, which broadens the scope of applications for these propellants [28, 34, 35]. Table 1.2 below presents a comparison between these propellants.

1.4 Electrically Controlled Propulsion

Electrically controlled propulsion is not a new or novel concept, as forms of electric propulsion have been implemented in spacecraft propulsion since the 1960s [37]. Generally, something that is electrically controlled is defined fundamentally as a propulsion system in which control

Table 1.2: Spacecraft monopropellant performance comparison. Evaluation calculated with NASA CEA code at 2 MPa chamber pressure with an expansion ratio of 50. Densities reported at 25 °C [19, 21, 23, 28, 29, 32, 33, 36]

Propellant	I_{sp} [s]	Density [g/cm^3]	ρI_{sp} [sg/cm^3]	Flame Temp. [K]
Hydrazine	236	1	247	1120
SHP-163	255	1.41	335	2400
AF-M315E	256	1.49	330	2160
LMP-103S	252	1.24	312	1880
FLP-106	259	1.36	353	2050

is managed through electrical signals. This very broad definition has applications in many industries, ranging from electric vehicles and locomotives to spacecraft propulsion systems. Typically, electric propulsion in spacecraft applications is done in the form of ion thrusters, Hall effect thrusters, or plasma thrusters. These thrusters generally utilize an electric and/or magnetic field to accelerate a charged particle, which produces small amounts of thrust. They are widely used in small-scale spacecraft thrusters due to their large I_{sp} and low mass; however, classic electrical propulsion differs greatly from electrically controlled propulsion. Electrically controlled propulsion refers to the decomposition of propellants via electrolysis.

1.4.1 Electrolysis of Propellants

Electrolysis in propellant refers to the electrochemical decomposition of ionic materials with the application of a voltage potential. HAN based propellants have been looked at since the 1980s to ignite electrically through electrolysis. Potential benefits of ignition in this manner is the ability to reduce ignition temperature, increased control and reusability, and reduced power requirements compared to a thermally ignited propellant [38].

1.5 Motivation

Increasing efforts have been made to create a suitable substitute to hydrazine based propellants due to their toxicity and various transportation hazards. In addition, furthering capabilities leads to increased propulsive requirements, necessitating smaller and more powerful propulsion systems. High density, non-toxic propellants with the easy ability to throttle and control provide a strong fundamental step in advancing propulsion systems. This combination of attributes is being explored in the form of electrically controlled gel propellants composed of a gel polymer electrolyte. This propellant decomposes and ignites through electrolysis with the addition of an applied voltage. Further, electrolytic combustion potentially mitigates prior drawbacks to gel propellants, in poor combustion efficiency.

The primary objective of this research was to explore the ignition characteristics and fundamental properties of electrically controlled gel propellants (ECGPs). An initial sweep of fuel to oxidizer ratios led us to a favorable formulation. From here, the impact of electrode surface area ratios and configurations, and combustion characterization, was completed by observing ignition characteristics as a voltage potential is applied. Materials characterizations were conducted through FTIR-ATR analysis and a thermal analysis (DSC/TGA) to characterize both chemical makeup and thermal decomposition.

Chapter 2

Review of Literature

This chapter introduces the difficulty of solid rocket motor controls and describes the use of electrically controlled combustion. This focus originates in an introduction to electrochemistry, which then goes into the use of energetic ionic liquids. The differences in thermal and electrolytic decomposition mechanisms are explored. It then focuses on the application of solid and gel electrically controlled propellants through polymer electrolytes, and a discussion on the decomposition of the ionic salt oxidizers used. Finally, a discussion on the classical gel propulsion efforts.

2.1 Solid Rocket Motor Control

Since the advent of solid rockets, achieving in-flight control has been a longstanding challenge. Early methods relied on indirect techniques, such as adjusting chamber pressure and grain profile, to influence the propellant's burn rate. However, modern solid rocket motors have introduced more advanced control mechanisms through the use of pintles and variable nozzle geometries.

A pintle is an actuator inserted into the nozzle throat to modulate its area, allowing for precise thrust adjustment during flight. While effective, pintle nozzles present several drawbacks. They are positioned at the point of highest heat flux within the engine, which imposes strict material requirements, as the pintle must withstand extreme temperatures without ablating to maintain its shape [1, 39, 40]. Additionally, the electronics and hydraulic actuators required for pintle movement must also be protected from these harsh conditions, increasing system complexity and weight. To address these challenges, an alternative approach involves directly controlling the propellant's burn characteristics through electrical modulation. This method could offer a more efficient and reliable means of thrust control while mitigating the thermal and mechanical issues associated with pintle nozzles.

2.2 Introduction to Electrochemisty

According to Patel, ”Electrochemistry is the study of electron movement in an oxidation or reduction reaction at a polarized electrode surface.” [41]. Central to this field is the transport of ions within an electrolyte, a process governed by the interplay of electric fields, concentration gradients, and solvent/ion interactions [42]. Ion mobility, defined as the proportionality constant between an ion's drift velocity and the applied electric field, is a key parameter influencing ionic conductivity, electrochemical reaction kinetics, and the performance of devices such as fuel cells, batteries, and electrochemical sensors. The understanding of ion mobility is essential for charge transport mechanisms in both dilute and concentrated electrolyte solutions. The motion of ions in an electrolyte occurs through migration and diffusion. Migration describes the movement of ions due to an external electric field, while diffusion arises from a chemical potential gradient, formalized by Fick's laws. Where Equation 2.1 describes the ionic drift velocity (u) as a function of ion mobility (μ) and electric field strength (E).

$$u = \mu E \tag{2.1}$$

The Nernst-Einstein relation establishes a direct link between ion mobility (μ) and the diffusion coefficient (D) in Equation 2.2.

$$\mu = \frac{DzF}{R_u T} \tag{2.2}$$

Where z is the ionic charge, F is the Faraday constant, R_u is the universal gas constant, and T is the absolute temperature. This relation highlights the fundamental dependence of ion transport on thermodynamic parameters. According to Bockris and Reddy [43], in highly dilute solutions where interionic interactions are negligible, ionic transport follows Kohlrausch's Law of Independent Migration, Equation 2.3, which states that the molar conductivity of an electrolyte is the sum of the contributions of its individual ionic species.

$$\Lambda_m = \lambda_+ + \lambda_- \tag{2.3}$$

Here, λ_+ and λ_- are the limiting molar conductivities of the cation and anion, respectively. This principle is valid under conditions where ion-ion interactions are sufficiently weak that each ion behaves independently in its contribution to the overall conductivity. However, at greater concentrations, deviations from ideal conditions arise due to ion pairing and electrostatic interactions, necessitating the use of the Debye-Hückel-Onsager theory. This model incorporates electrophoretic and relaxation effects, which reduce ion mobility by modifying the local ionic atmosphere. The electrophoretic effect results from the movement of the ionic cloud in opposition to the field-driven motion of the central ion, while the relaxation effect stems from the asymmetric redistribution of the ionic atmosphere following ion displacement [44]. The Onsager equation provides a correction to Kohlrausch's Law for strong electrolytes in Equation 2.4.

$$\Lambda_m = \Lambda_m^o - (A + B\Lambda_m^o)\sqrt{c} \tag{2.4}$$

Here, A and B are constants dependent on temperature, dielectric constant, and viscosity of the solvent, and c is the electrolyte concentration. This equation was again amended in 1957 by Raymond Fuoss, a student of Onsager, to develop a higher-order mathematical model to describe the theory presented in Onsager's physical model [44]. The application of this equation is critical in accurately predicting conductivity in practical electrochemical systems. Solvation also plays a pivotal role in determining ion mobility, as highlighted by Koryta and Kavan [42]. The effective radius of an ion in solution is not solely dictated by its crystallographic size but is significantly influenced by its hydration shell. Highly charged and small-radius ions, such as Li^+, exhibit extensive hydration, which increases their Stokes radius and decreases their mobility relative to larger, less hydrated ions like Cs^+. The solvent's viscosity (η) further impacts ionic motion, as reflected in the Stokes-Einstein relation in Equation 2.5.

$$D = \frac{k_B T}{6\pi\eta r} \tag{2.5}$$

Where k_B is the Boltzmann constant and r is the hydrodynamic radius of the solvated ion. The viscosity dependence is particularly relevant in non-aqueous electrochemistry, where solvents of varying dielectric properties modulate ion transport behavior. A comprehensive understanding of ion mobility is crucial for optimizing electrochemical devices. In electrolyte based propellants, for instance, ion mobility dictates the ionic conductivity, which is a primary determinant of ignition and performance. The theoretical and experimental study of ion mobility remains an active area of research, with implications extending from energy storage technologies to biophysical electrochemistry and propellant performance.

2.3 Introduction to Electrically Controlled Propellants

In 1964, Mayo et al. proposed the idea of utilizing electrical stimuli to control solid propellant combustion [45]. His study focused on an aluminized solid propellant exposed to a voltage potential in the gas phase, where he demonstrated that an electric potential parallel to the surface of the burning surface did not impact the burn rate of the propellant, but an electric potential orthogonal to the burning surface increased the burn rate. In addition, it was also shown that the polarity of the electric potential also impacted the burn rate of the propellant [45]. Work by the United States Air Force in the 1970s also investigated electric control of propellants, where they demonstrated that an applied electric field can significantly influence the combustion characteristics of solid propellants, with effects dependent on electrode configuration, propellant composition, applied voltage magnitude and polarity, and chamber pressure. Burning rate augmentation was primarily attributed to Joule heating from electrical breakdown currents, which preheated the propellant surface and enhanced decomposition kinetics. Conversely, burning rate suppression was observed under conditions where flame electrons were diverted or neutralized by the applied field, disrupting the energy feedback mechanisms necessary for steady combustion. The observed effects highlight the complex interplay between electrostatic forces, plasma dynamics, and propellant combustion processes [46]. More recently, Young et al. identified an inverse relationship between the regression rate of a solid fuel and the applied DC voltage. This phenomenon was attributed to the disruption of heat feedback to the propellant by the ionic wind effect [47].

2.3.1 Ionic Monopropellants

As mentioned in Chapter 1, hydrazine and its derivatives have been the backbone of monopropellant propulsion since being introduced in the 1960s [19]. The introduction of the catalyst, Shell 405, is considered to have made hydrazine based propellants practical due to its much reduced ignition time [12, 48]. Hydrazine, N_2H_4, follows a two-step decomposition process into products of ammonia, nitrogen, and hydrogen, shown in Equations 2.6 and 2.7 [49].

$$N_2H_4 \rightarrow \frac{4}{3}NH_3 + \frac{1}{3}N_2 \tag{2.6}$$

$$NH_3 \rightarrow (1-x)NH_3 + \frac{1}{2}N_2 + \frac{3}{2}xH_2 \tag{2.7}$$

Here, x represents the amount of dissociation of ammonia, NH_3, which was found to impact the performance of the propellant [12, 49]. Greater dissociation of ammonia was found to negatively impact the I_{sp} and flame temperature, reducing performance because the dissociation is exothermic. Early development of Shell 405 found that the catalyst would typically increase dissociation, yet advances in the last 50 years have been able to mitigate this impact [12]. Nonetheless, toxicity and high associated costs of hydrazine and its derivatives, including MMH and UDMH, have motivated a search for alternatives, which have largely turned to ionic liquid propellants based on ADN or HAN [19, 20, 21, 29, 50]. These alternatives offer similar performance and lower toxicity, in addition to generally lower freezing points [19, 21, 29, 51]. Typical applications of hydrazine employ a catalytic or thermal ignition process; however, due to the ionic nature of EILs, electrolytic ignition methods can be explored. The following sections will discuss the development of ADN- and HAN- based propellants, including a discussion on these decomposition methods. Discussion will then turn towards the development of electrolytes for use in electrically controlled propellants (ECPs).

Thermal and Catalytic Methods in IL Monopropellants

HAN is primarily employed in a strong aqueous solution for energetic applications. This makes the solution an ionic liquid due to its dissolved and charged hydroxyl-ammonium ions and nitrate ions present in the solution. HAN is typically utilized in this form due to it being an explosive crystalline solid, and extremely hygroscopic in its pure form [52, 53]. The thermal decomposition of the aqueous HAN solution is initiated by a proton transfer reaction as indicated in Equation 2.8.

$$[NH_3OH]^+[NO_3]^- + H_2O \rightarrow NH_2OH + HNO_3 + H_2O \tag{2.8}$$

This proton transfer is the rate-limiting factor, as large amounts of energy go into this reaction during thermal decomposition [54]. Therefore, a catalytic decomposition is typically used to reduce the required energy requirement for decomposition [51]. Catalytic decomposition in general faces challenges in monopropellant applications as the catalyst must be able to withstand high temperatures and be relatively non-ablative to increase durability and lifespan. In addition, the catalyst must provide sufficient energy to ignite the monopropellant, or else high preheat temperatures are required to achieve ignition [51]. Shell 405 has proven to have low degradation, allowing for use after an exposure time of over an hour. Further, it provides sufficient energy for ignition at low temperatures [12, 50]. Unfortunately, typical catalysts have a temperature stability limit around 1500 K, which is acceptable for use in hydrazine based propellants due to their low flame temperature; however is unsuitable for ADN and HAN based propellants due to their higher flame temperatures [24, 28, 29, 55]. These high temperatures lead to oxidation, sintering, and surface loss of the catalysts, which results in the catalyst's deactivation, leading to poor performance and large ignition times [35]. Due to this, alternative catalysts are required for use in HAN and ADN based propellants.

The development of catalysts for (HAN) monopropellant decomposition has progressed through investigations into both catalytic efficiency and long-term stability. A study by Courtheoux et al. in 2005 [56] examined the thermal and catalytic decomposition of HAN and hydrazinium nitroformate (HNF) using a Pt/Al O -Si catalyst, where the platinum acts as an activator with the silica-alumina catalyst. The results demonstrated that high-concentration HAN solutions (up to 79% wt.) exhibited enhanced decomposition efficiency with catalysis significantly lowering the decomposition temperature and increasing gas yield. However, commercial HAN solutions containing stabilizers showed reduced catalytic performance, indicating the necessity of optimizing propellant formulations to maximize reactivity. More recently, Amrousse et al. [35] advanced this research by evaluating iridium-based catalysts under monopropellant thruster conditions, with a focus on performance degradation over time. While iridium catalysts demonstrated high initial activity, oxidation and severe sintering led to progressive deactivation, highlighting the challenges associated with long-term operational stability. Nonetheless, catalytic decomposition of HAN and ADN based propellants were proved effective as the thermal decomposition temperature of their HAN and ADN formulations were 152 °C and 116 °C respectively. These temperatures were reduced greatly to 47 °C and 51 °C, with the use of a catalyst [51]. Further research on ADN based propellants FLP-106 and LMP-103S were conducted through the RHEFORM project, which sought to find a suitable catalyst that meets performance requirements and consists of materials readily available, such that the required materials are not faced with ITAR restrictions [55, 57]. Development investigated both granulated and monolithic catalysts, based on platinum and copper, which brought the decomposition temperature down from around 140 °C to around 110 °C, leaving room for improvement [57]. Additionally, monolithic catalysts demonstrated increased mechanical properties and showed stability in a 1200 °C environment for extended periods and up to 1500 °C for short exposure times [34]. Nonetheless, the limiting factor in the decomposition is the water concentration, as noted in initial ADN and

HAN catalytic decomposition experiments. The water in the above propellants is required to evaporate out of solution before decomposition or ignition could occur, thus, it was deduced that poor ignition qualities resulted from heat transfer from the ignition source into the propellant [58]. Due to this, a thermal ignition of these IL monopropellants requires large amounts of energy [56]. Efforts are ongoing to develop an effective catalyst for IL propellants, with progress moving towards reducing the required catalyst preheat temperature, and increasing their effective lifespans; however, due to the ionic nature of these propellants, electrolytic decomposition and ignition methods are being explored as well [54].

Electrolytic Decomposition in IL Monopropellants

Electrolytic decomposition of HAN follows a different decomposition process than the aforementioned thermolysis or catalysis. Decomposition occurs at both the anode and cathode and demonstrates different reactions due to the polarities of the ions and electrodes. At the anode, the liquid water is electrolyzed, producing protons and electrons as shown in Equation 2.9. The formation of this proton promotes the further decomposition of the HAN at the anode depicted in Equation 2.10 [59].

$$H_2O \rightarrow \frac{1}{2}O_2 + 2H^+ + 2e^- \tag{2.9}$$

$$[NH_3OH]^+[NO_3]^- + H^+ \rightarrow HNO_3 + [NH_3OH]^+ \tag{2.10}$$

This produces an overall electrochemical reaction seen below at the anode side (Equation 2.11).

$$2[NH_3OH]^+[NO_3]^- + H_2O \rightarrow \frac{1}{2}HNO_3 + 2[NH_3OH]^+ + 2e^- \tag{2.11}$$

In this decomposition, there is a large composition of $[NH_3OH]^+$, so it migrates toward the cathode where it is reduced as followed in Equation 2.12 [59].

$$2[NH_3OH]^+ + 2e^- \rightarrow 2NH_2OH + H_2 \tag{2.12}$$

Combining the general reaction at both the anode and cathode (Equations 2.11 and 2.12) gives the global reaction in the electrolytic decomposition of HAN shown below in Equation 2.13 [59].

$$2[NH_3OH]^+[NO_3]^- + H_2O \rightarrow 2HNO_3 + 2NH_2OH + H_2 + \frac{1}{2}O_2 \tag{2.13}$$

Early experiments with electrolytic decomposition of HAN-based IL monopropellants were in liquid gun propellants by the U.S Army, where it was concluded that the magnitude of the applied voltage impacted the ignition delay of the sample. Additionally, the polarity of the electrodes, the electrode materials, and the relative surface areas of the electrodes influenced the energy required to decompose and ignite the propellants [60]. More recent focus on electrolytic control of HAN-based propellants has been considered for micro-scale thrusters by Yetter et al., utilizing a propellant consisting of HAN, AN, and methanol [61]. It was found that the resistance of the propellant, and subsequently the conductivity, was time dependent during the decomposition process, and noted a voltage dependency in that higher applied voltages increased gasification [61]. Additionally, Yetter and Wu constructed a microthruster utilizing parallel plate electrodes to take advantage of HAN electrolytic decomposition [62]. This study indicated that increasing the voltage did not necessarily decrease the ignition delay time, but they did note that increasing the molar concentration of HAN, effectively reducing the water content and increasing ion density, led to a higher reaction temperature. Further, the peak current draw was correlated to the maximum thrust, indicating the largest rate of decomposition at this peak [62].

The electrolytic decomposition of HAN typically generates a sharp rise in current, followed by a substantial drop [61, 63, 64]. In this system, the current is indicative of the ion transport within the propellant, therefore, a drop in current indicates a reduction of ion transport. In a static environment, surface area is impacted as decomposition continues, however, Chai et al. noted this reduction in current is due to nitrate adsorption onto the surface of the electrode, inhibiting ion transport [63]. Additionally, the electrode materials significantly impact the decomposition of HAN, and Chai et al. reported classes of inert and sacrificial electrodes. Graphite and titanium were noted to be inert electrodes, whereas copper, aluminum, platinum, and nichrome are sacrificial electrodes that erode over time. The sacrificial electrodes performed better, and both the current and observed temperature were greater for aluminum and copper electrodes compared to graphite [54, 65]. Thus, the decomposition is sensitive to the electrode material, suggesting that the electrodes themselves may be involved in the overall decomposition reaction [61]. Additionally, Khare et al. modeled the electrolytic decomposition process of various aqueous HAN solutions, finding that increasing initial temperature, HAN concentration, or current reduces the ignition delay time [59].

2.3.2 Polymer Electrolytes

Generally, a polymer electrolyte (PE) is any sort of polymer matrix that is polar, meaning it is capable of electron donation, and thus capable of ion conduction [66, 67, 68]. Typical polymers utilized in PEs are polyvinyl alcohol (PVA), polymethyl methacrylate (PMMA), and polyethylene oxide or polyethylene glycol (PEO/PEG), where the mechanical properties of the resulting electrolyte are dependent on the structure and molecular weight of the polymer [69]. To create the PE, ionic salts are dissolved into the polymer, typically through a solvent. The degree of crystallinity within the polymer matrix impacts the ionic mobility of the electrolyte, influencing the conduction when a voltage is applied [68, 70]. Additionally, the morphology and glass transition temperature of the selected polymer further impact the ionic response in the electrolyte [67, 71]. Multiple modes of ion transport are believed to exist, dependent on the material properties of the polymer used. In crystalline polymer electrolytes, the organized structure of polymer chains facilitates the formation of inter-chain ”tunnels,” allowing the ion of interest to hop between coordination sites while the counterion migrates along the polymer chain [72]. These tunnels enable selective control over anion and cation transport, as the highly ordered crystalline domains preferentially permit the passage of one ion while excluding its counter ion, thereby facilitating ion separation [73]. This selective transport mechanism can enhance the conductivity of crystalline polymer electrolytes. In contrast, amorphous polymers that exhibit enhanced conductivity are proposed to do so due to their disordered nature, which increases chain mobility. This greater molecular flexibility allows for transient ion coordination, thereby improving ion mobility [72, 74].

In our case, polymer electrolytes can be categorized into solids and gels depending on viscosity. Solid polymer electrolytes (SPEs) are created through the coordination of the salt into the polymer matrix to form a complex [68, 75]. Under an applied voltage, this complex is broken, resulting in an ion exchange. Typical gel polymer electrolytes (GPEs) are created using PEG in the amorphous domain. It is noted that these polymers oftentimes absorb substantial amounts of solvent, and that solvent selection impacts the ionic conductivity of the electrolyte based on their dielectric constant [72]. PEO and lithium-based electrolytes have the most literature pertaining to the GPEs due to their research and potential application in lithium-ion batteries [76, 77]. In both cases, additives can be added, often carbon or aluminum, to increase both conductivity and propellant performance [68].

2.3.3 Electrically Controlled Solid Propellant

Recent focus on the electrolytic decomposition of propellants has been on solids. This approach has several advantages over gas phase control previously discussed, since it has a direct effect on the decomposition behavior. In this manner, an application of a voltage potential can induce and impact the electrochemical reactions rather than more loosely influence the gas transport. Further, electron and ion transport properties of a condensed phase electrolyte allow for a current to flow and joule heating, providing additional energy to the propellant, accelerating the decomposition.

Initial efforts in creating a conductive solid propellant came from Digital Solid State Propellant (DSSP) using AN and HAN as oxidizers. Their first formulation, ”ASPEN” utilized AN as the primary oxidizer and proved to successfully ignite, achieving an I_{sp} of around 225 sec. A new formulation was introduced with HAN as the oxidizer and PVA as the polymer, with the motivation to increase the conductivity of the propellant to reduce ignition delays [78, 79]. This formulation became known as ”HIPEP” for High Performance Electric Propellant and achieved an I_{sp} of 245-263 seconds depending on the aluminum content [78]. Despite the new formulation, HIPEP was only viable in micro-thruster applications due to its sensitivity to electrode spacing. Further research on PVA/HAN based solids have been conducted by the likes of Hiatt and Frederick [80], who studied the impact of electrode configuration on HIPEP. They found that the ignition location was dependent on both the electrode configuration and the area ratio between the cathode and anode [80]. However, parallel plate configurations saw ignition favor the anode [80]. Further attempts to increase the conductivity of such propellants were undertaken by Bao et al., who considered the impact of an additive in PVA/HAN propellants. They introduced small concentrations of multi-walled carbon nanotubes (MWCNTs) and aluminum. The introduction of MWCNTs and micron sized aluminum powder increased the conductivity of the propellant in the solid phase, however, the use of nano aluminum decreased the solid phase conductivity [81, 82]. This decrease in conductivity was explained as an interaction between the nano aluminum powder and water in the sample during the curing phase, which, when cured, reduced the total amount of water in the sample, thus decreasing conductivity [81]. In a later study, Bao et al. found that including graphite can also increase conductivity and that the inclusion of these additives decreases the pressure deflagration limit due to an increase in thermal conductivity and heat release from the additives [81, 83]. Additionally, the conductivity of the sample in the solid phase was seen to be dependent on the concentration of solvent that remained in the sample after preparation [81], and Whalen et al. demonstrated that additives can be incorporated into ECSPs to increase conductivity in the solid phase. They noted that ignition delay is correlated to the magnitude of the applied voltage and that electrolytic decomposition advanced faster than a purely thermal mechanism, indicating the importance of conductivity and electrochemistry in ECSPs. [84].

Perchlorate oxidizers are also considered, with the majority of research coming in the form of AP and LP due to their high oxygen content and higher decomposition temperatures [85, 86, 87]. Gobin et al. utilized AP/LP co-oxidizers and noted that a melt layer was required for the propellant to be conductive and thus ignite [88, 89]. AP does not form a highly conductive melt layer as it decomposes and sublimates into gaseous products instead [89, 90, 91]. Zamir et al. utilized AP as the sole oxidizer and found that the burn rate was relatively unaffected by the magnitude of applied voltage [90].

A PVA/LP propellant study completed by He et al. demonstrated a burn rate dependency on the magnitude of the applied voltage [85]. This study also showed that concentrations of residual solvent in the sample impacted the performance of the propellant, which, along with Bao et al., suggests that controlling the variability of residual solvent concentration is pertinent in experimental consistency. Contrary to AP-based propellants, experimentation indicated that LP-based propellants are sensitive to applied voltage, altering ignition times [82, 92, 93, 94]. Li et al. demonstrated that ignition characteristics of LP based ECSPs are influenced by the electrode area ratio, surface roughness of the electrode, and the electrode material [94]. In these experiments, the propellant ignition correlated to a current peak, followed by a sharp drop after ignition, explained as an Arrhenius relation between the temperature and the conductivity of the propellant. The propellant is heated under an applied voltage, and the conductivity increases, leading to a larger current up until ignition. The expression for conductivity is given in Equation 2.14 [86, 95, 96].

$$\sigma(T) = \sigma_o exp(\frac{-E_a}{kT}) \tag{2.14}$$

Where σ is the electrical conductivity, E_a is the activation energy, k is the rate constant, and T is the temperature.

2.3.4 Ionic Salt Decompostion

For application in propellants, the nitrate and perchlorate families are widely used due to their high bond energies and crystalline structure [97]. It should be noted, however, that the electrolytic decomposition process of these salts is different from their thermal decomposition process. Due to the use of a solvent to create polymer electrolytes, the salts first undergo a dissolution process defined in Equations 2.15 and 2.16. Selected reactions are for AN and

LP as examples, however, all oxidizer salts behave similarly.

$$NH_4NO_3 \rightarrow NH_4^+(aq) + NO_3^-(aq) \tag{2.15}$$

$$LiClO_4 \rightarrow Li^+(aq) + ClO_4^-(aq) \tag{2.16}$$

Once the salts have dissolved into their respective ions, they are charged and undergo decomposition when a voltage potential is applied. The anions oxidize at the anode, whereas the cations move toward the cathode, where they are reduced. Oxidation of the nitrate anion is shown in Equation 2.17 and the oxidation of the perchlorate anion is shown in Equation 2.18 [98, 99].

$$NO_3^- \rightarrow NO_2 + \frac{1}{2}O_2 + e^- \tag{2.17}$$

$$ClO_4^- \rightarrow \frac{1}{2}Cl_2 + 2O_2 + e^- \tag{2.18}$$

At the cathode, the cations are reduced, with the lithium shown in Equation 2.19, and the ammonium ions described in Equations 2.20 and 2.21 [99].

$$Li^+ \rightarrow e^- + Li \tag{2.19}$$

$$3NH_4^+ + 3e^- \rightarrow \frac{3}{2}H_2 + 3NH_3 \tag{2.20}$$

$$2H^+ + 2e^- \rightarrow H_2 \tag{2.21}$$

2.4 Gel Propellants

Gelled propellants have been of interest in propulsive applications since the 1970s due to their favorable safety factors and comparable performance compared to conventional liquid propellants [26, 100, 101]. Gelled bipropellants have demonstrated use in hypergolic ignition schemes as the required catalyst can be suspended within the gel to facilitate ignition [102, 103]. Nonetheless, gel propellants suffer from poor combustion performance due to difficult atomization and injection difficulties [100, 104, 105]. Due to this, there have been many studies on the characteristics of gel propellant combustion [104, 105, 106, 107]. In the 1990s, Nachmoni et al. utilized a gelled JP-5 fuel and noted that their gel followed the d^2-law, which describes droplet evaporation and combustion, and which relationships are shown in Equations 2.22-2.24 [105, 106]. These relations connect the initial diameter of the droplet d_o^2 to the burning time t_b through a burn rate coefficient K.

$$d_d^2(t) = d_o^2 - Kt \tag{2.22}$$

$$K = \frac{8D\rho_g}{\rho_d} ln(1 + B) \tag{2.23}$$

$$t_b = \frac{d_o^2}{K} \tag{2.24}$$

Here, D is the oxygen diffusivity, ρ_g is the density of the gas off of the droplet as a result of combustion or evaporation, and B is the Spalding mass transfer number. The Spalding number is often times assumed to be unity, implying that the fuel vaporization rate at the surface of the droplet is equivalent to the fuel consumption rate of the flame [108]. However, the burn rate coefficient, K is only constant under an assumption of steady state temperature at the surface of the propellant [106]. Arnold et al. carried out similar experiments with JP-8 and fumed silica as a gellant. They found that increasing the gellant concentration caused a deviation from the d^2-law, and that at these higher concentrations of silica, there was incomplete combustion resulting in unburnt silica. This resulted in both combustion instabilities and a non-uniform temperature across the surface of the droplet [106]. More recently, Cao et al. also studied a gelled kerosene fuel with fumed silica and characterized the combustion of the droplets in a manner different than past experiments. During the initial stages of the burning process, they noted that a silica shell formed, which encapsulated the fuel. The shell then sheds and shrinks as the fuel vaporizes. When the pressure inside the shell increases, the shell breaks apart, and then the droplet combusts. Similar to past studies, the droplets were seen to follow the d^2-law at lower concentrations of silica; however, they deviated from the law at higher concentrations of gellant [107]. Challenges in the combustion and atomization of gelled propellants have remained key limitations to their practical application. In recent years, an alternative approach has emerged from ongoing research into electrolytic ignition methods for monopropellants and polymer electrolytes. Due to their ionic conductivity and electrolytic decomposition, polymer electrolytes show promise as ECPs in both gel and solid states.

Chapter 3

Methods

This chapter discusses material preparation and the experimental methods utilized to study electrically driven decomposition and combustion.

3.1 Materials

The ECGPs were composed of PEG, AP, and LP, using methanol as a solvent. The PEG was purchased from Sigma Aldrich with an average molecular weight of 400 g/mol. The AP was purchased from Firefox Enterprises with a stated particle size of 90 μm, and from Pyro Chem Source with a particle size of 90 and 200 μm. The methanol was purchased from Fischer Chemicals with a stated purity of 99.9%. The LP was purchased from Fischer Scientific and had a stated purity of over 99%. To establish a baseline, theoretical performance was estimated using NASA's Chemical Equilibrium with Applications (CEA) code [109]. The analysis utilized the rocket problem solver with a chamber pressure of 6.8 atm, an exit expansion ratio of 100, and equilibrium properties. Typically a binary composition of a polymer and AP has been unsuccessful, as noted, because the AP does not form the melt layer required for increased conductivity. Due to this, LP is often included as an oxidizer to increase conductivity and response, however, this tends to decrease performance, as seen in Fig. 3.1, where the overall fuel to oxidizer ratio is held constant, but the ratio of AP to LP is varied. As seen, the inclusion of LP generally lowers the performance of the propellant, indicated by a lower I_{sp}.

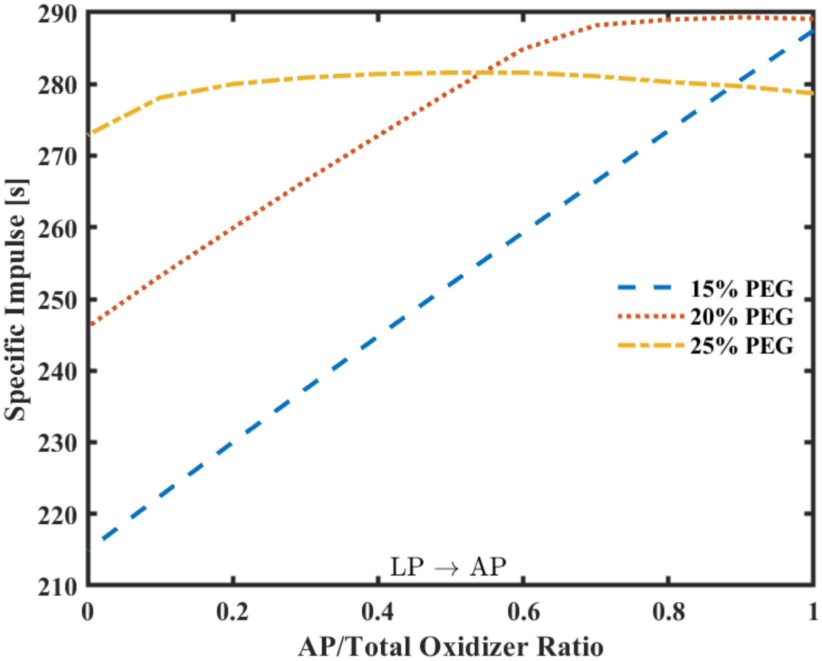

Figure 3.1: I_{sp} of PEG Based Propellant as a Function of AP/LP Ratio

Additionally, we analyzed the theoretical performance of a PEG/AP propellant across different fuel mass ratios to determine an initial step for experimentation. Shown in Fig. 3.2 are the flame temperatures and I_{sp} of this formulation, with a stoichiometric ratio containing 17 wt% fuel. A sweep of fuel ratios was conducted where it was decided that 20 wt% PEG and 80 wt% AP provided the best compromise between propellant performance and mechanical characteristics. Additionally, monopropellant hydrazine is provided as a reference, indicating significantly higher performance in the range of electrically controlled propellants.

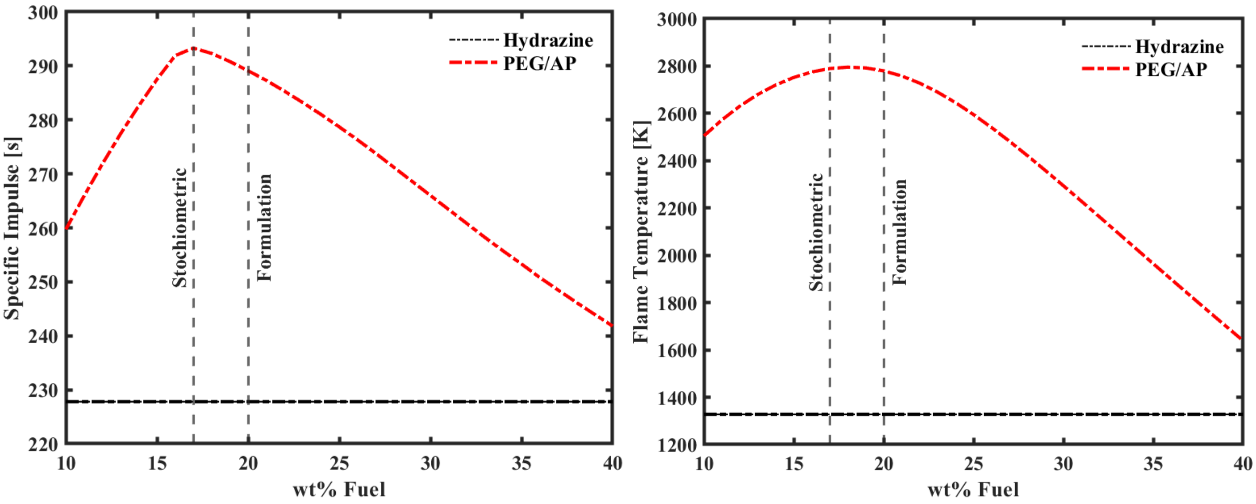

Figure 3.2: Flame Temperature and Specific Impulse of PEG/AP ECGP

3.2 Propellant Synthesis

Gel propellants investigated utilized PEG and AP and/or LP at near stoichiometric mixtures. An initial panel of propellants were tested with their compositions summarized in Table 3.1. The proposed propellants were initially experimented on to find a formulation which provided a preferable electrical response and mechanical properties. Initially, for these comparisons, the PEG content was held constant at 25 *wt*% and the relative concentration of AP to LP was varied. A secondary panel that utilized only AP as the oxidizer varied the concentration of PEG to AP from 20 *wt*% to 30 *wt*% PEG. Finally, a study was conducted with ethylene glycol (EG), with the primary motivator to reduce the propellant viscosity, where two formulations were tested. The propellants were prepared through a solution casting method in methanol. In this method, the propellants are prepared by first adding methanol to a beaker while stirring it continuously on a hot plate set to 40°C. PEG was then slowly added into the solution and allowed to dissolve for 1 hour, then the AP/LP was slowly added to the solution. Once the oxidizer was added, the propellant was covered and stirred for 24 hours under heat.

After 24 hours, the covering was removed to allow any remaining methanol to evaporate. Once sufficient methanol was removed from the sample and the propellant became too viscous such that the stir bar seized, the sample was removed from the hot plate and placed in the vacuum oven. The solution remained in the vacuum oven set at 40°C and 13 kPa for another 24 hours. Upon completion, the propellant was stored under vacuum until utilized in experiments to avoid any moisture absorption. A diagram of this process is shown in Fig. 3.3.

Table 3.1: Compositions of PEG Gels

Propellant ID	*wt*% Fuel	*wt*% AP	*wt*% LP
PEG25AP100	25	75	0
PEG25AP50LP50	25	37.5	37.5
PEG25LP100	25	0	75
PEG20AP100	20	80	0
PEG30AP100	30	70	0
EG20AP100	20	80	0
EG25AP75LP25	25	56.25	18.75

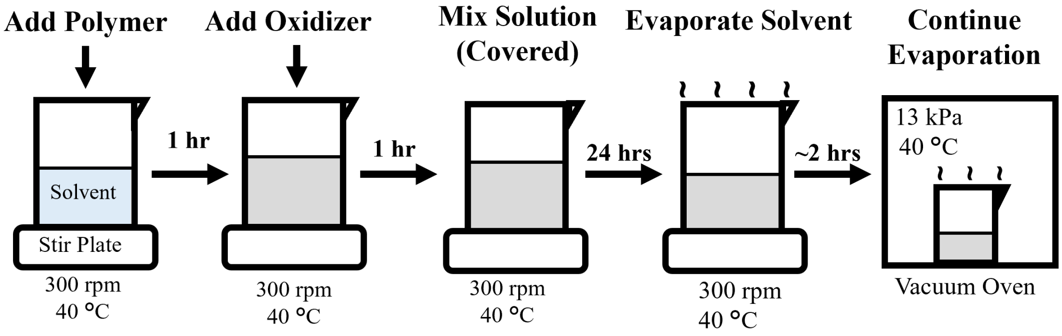

Figure 3.3: ECGP Preparation Schematic

3.3 Thermal Decomposition Characterization

The ignition and combustion processes of ECPs generally involve a competition between electrochemistry and thermal decomposition and thus it is important to characterize the thermal decomposition process for a complete picture of the ignition and combustion process. The propellant and its constituent oxidizer and polymer were subjected to differential scanning calorimetry (DSC) and thermogravimetric analysis (TG) using a Netzsch STA 449 F5 Jupiter simultaneous thermal analyzer. The analysis used a heating rate of 10 °C/min in a nitrogen purged environment from 25 °C to 450 °C.

3.4 Materials Charicterization

To verify complexation of the polymer and oxidizer, the propellant and its constituent components were studied using an attenuated total reflectance (ATR) sampling methodology for Fourier transform infrared spectroscopy (FTIR). The material characterization analysis was conducted with a Varian 670-IR with mid-IR integrated sphere FT-IR spectrometer. Absorbance was measured at a spectral resolution of 4 cm^{-1} over a range of 4000 cm^{-1} to 400 cm^{-1}.

3.5 Ignition Experiments

To characterize the combustion characteristics of the ECGPs, a series of experiments were conducted under a voltage potential ranging from 125 V to 200 V. Electrode configurations were evaluated using both a parallel and concentric test apparatus. Copper electrodes were utilized in all experiments. The parallel electrode experiments were carried out in square borosilicate test tubes with an electrode spacing of 6 mm, as shown in Fig. 3.4. After the initial propellant panel, even length and offset electrode lengths were considered. Even-length electrode experiments were conducted with electrode lengths of 12.7 mm, 9.53 mm, and 6.35 mm, whereas the uneven electrode experiments used a short electrode at 6.35 mm, and a long electrode at 12.7 mm displayed in Fig. 3.4. Uneven electrode experiments were conducted with both polarities, which are referred to as a long anode and a long cathode configuration. The offset electrode experiments were carried out such that the total electrode surface area was the same as the even length electrodes of medium size (9.53 mm). In the parallel configuration, the electrodes were mounted flush with the top of the borosilicate tube along the walls protruding downward into the tube such that they were submerged in the propellant sample.

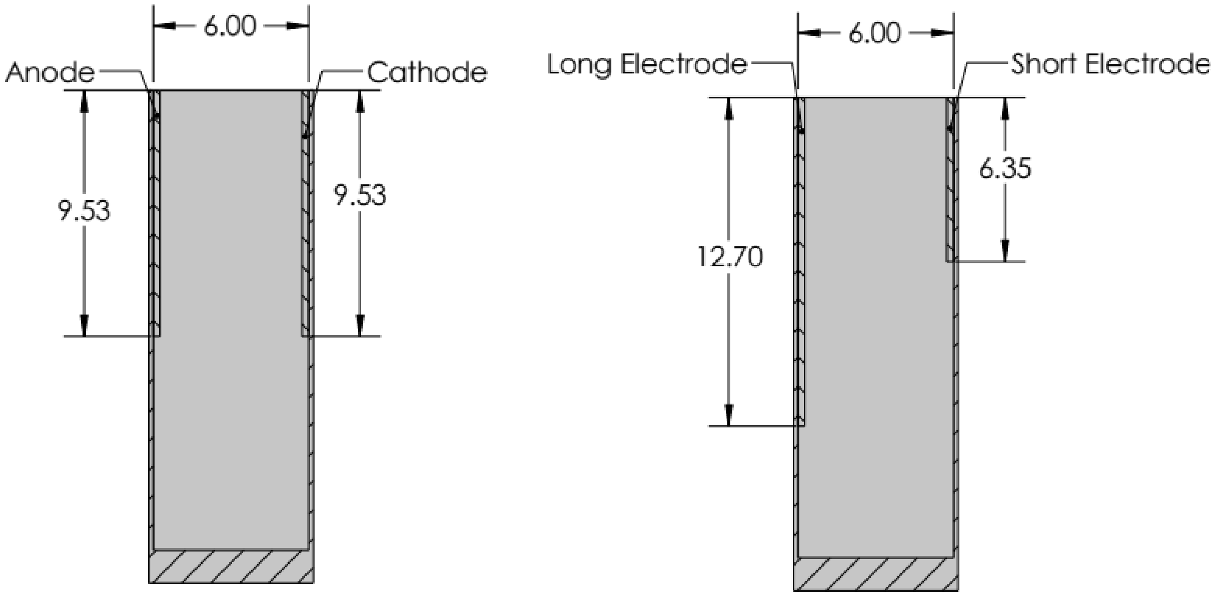

(a) Even Length Electrodes (b) Uneven Length Electrodes

Figure 3.4: Parallel Configuration Experimental Configuration

A second experimental (concentric electrodes) setup was included to study the impact that electrode orientation had on the propellant ignition behavior. The inner electrode had a 6.35 mm diameter, and the outer electrode had a 12.7 mm diameter as shown in Fig. 3.5 The outer electrode is press fit into the outer lip of the electrode holder while the central electrode is threaded, and set up in a jig to ensure concentricity before being screwed into the bottom of the electrode holder such that the electrode faces are parallel to each other. Concentric experiments were conducted with both polarities and are named the anode out and cathode out configuration, referring to the polarity of the outer ring electrode. A variation of the concentric configuration incorporated an insulating sleeve over a portion of the central rod electrode to reduce the surface area with minimal impact on the electric field is shown in Fig. 3.5. These configurations are referred to as the anode out and cathode out sleeved electrode, referring to the polarity of the outer ring and the sleeve on the inner rod electrode. The concentric geometry is the more likely geometry for application, while the parallel geometry allows us to study fundamental aspects of the ignition process more readily.

In either configuration, a constant voltage was applied from an ITECH 3902D-300-20 DC power supply. The voltage was measured directly from the power supply, and current was monitored using a Teledyne Test Tools T3CP100-2 current probe. A Vision Research Phantom VEO 710L high-speed camera and a FLIR X6983 thermal camera were used to record experiments, and both cameras were triggered simultaneously with the application of voltage. The FLIR thermal camera operated at a default emissivity of 0.92, and the high-speed footage settings varied, but were typically shot at one thousand frames per second. The high-speed footage was used to determine the ignition delay time, which was defined as the time between initial voltage application and the first observation of luminosity.

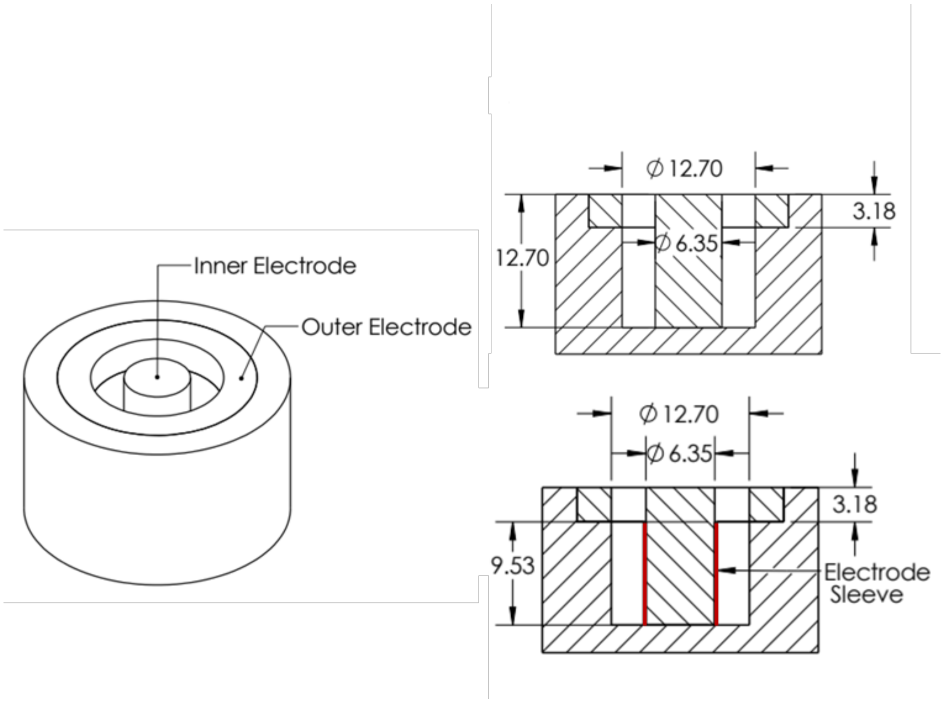

Figure 3.5: Concentric Electrode Experimental Configuration

3.6 Electric Field Analysis

An analysis of the electric field was conducted to help explain the ignition behavior through the different experimental configurations considered. The simulations were conducted using software from EM Works in SolidWorks using the geometries of the apparatuses used throughout the experiments. Electrical properties of copper were used for the electrodes and fused silica for the square tube and FR-4 garolite for concentric holder configurations as seen in Fig. 3.4 and Fig. 3.5. The resistance of the propellant during decomposition was estimated by taking the median value of the measured current and relating it to resistance through Ohm's Law. With the resistance and spatial constraints of the propellant, the electric permittivity can be calculated and is assumed constant through the simulation. The electric field, in this case, is a static problem defined in three dimensions. Equation

3.1 depicts the electric field equation in its simplest one-dimensional form for an electrolytic cell.

$$E = V/d \tag{3.1}$$

Where E is the magnitude of the electric field, V is the applied voltage, and d is the distance between the electrodes. Implemented in three dimensions, the electric field becomes the gradient of the electric potential as a function of distance, shown in Equation 3.2.

$$\vec{E}(\vec{r}) = -\nabla\phi(\vec{r}) \tag{3.2}$$

Where $\vec{E}$ is the electric field vector at position $\vec{r} = (x, y, z)$, $\phi(\vec{r})$ is the voltage, and $\nabla\phi$ is the gradient. Poisson's equation for electrostatics is used to solve this problem, where the permittivity of the medium is known. In this case, the permittivity of the electrodes and electrode holders are known through literature, and the permittivity of the propellant itself was calculated experimentally. Poisson's Equation is shown in Equation 3.3.

$$\nabla^2\phi(\vec{r}) = -\frac{\rho(\vec{r})}{\epsilon} \tag{3.3}$$

Here, the charge density, ρ, is solved for numerically, and the electric field can be calculated from the gradient. Additionally, boundary conditions are defined such that the anode is at the simulation voltage, 175 V in all cases, and the cathode is set to 0 V. The properties through the propellant were numerically calculated through a generated mesh utilizing a finite element method.

Chapter 4

Characterization Results

Thermal decomposition and materials characterizations were conducted on the propellant and its constituents. The propellant utilized in these tests consists of 20 wt% PEG and 80 wt% AP, and solution cast in methanol. This formulation was decided on through a panel of potential propellants, whose results were examined through ignition experiments covered in Chapter 5

4.1 Thermal Decomposition Characteristics

TGA and DSC analysis of AP, PEG, and a propellant sample formulated with 20 *wt*% PEG and 80 *wt*% AP are shown in Fig. 4.1. The propellant sample more closely follows the decomposition characteristics of AP due to the sample being 80 % oxidizer. An endotherm was observed at 240 °C in both the AP and propellant composition, which corresponds to the phase transformation of AP from orthorhombic to cubic [110, 111]. The exothermic peak observed with AP around 310 °C correlates with the primary mass loss in the TGA, which indicates the high-temperature decomposition of AP. PEG underwent a single-step decomposition beginning at around 230 °C as indicated in the TGA analysis. The propellant sample displays no mass loss near 65 °C, the methanol boiling point, indicating that the solvent was completely removed from the sample. This is an important result, as historically electrically controlled propellants contain residual solvent, which increases the conductivity of the propellant, making them susceptible to manipulation via a voltage potential. However, residual solvent reduces propellant performance in terms of specific impulse. Thus, if a functioning electrically controlled propellant can be manufactured with no residual solvent performance can be maximized.

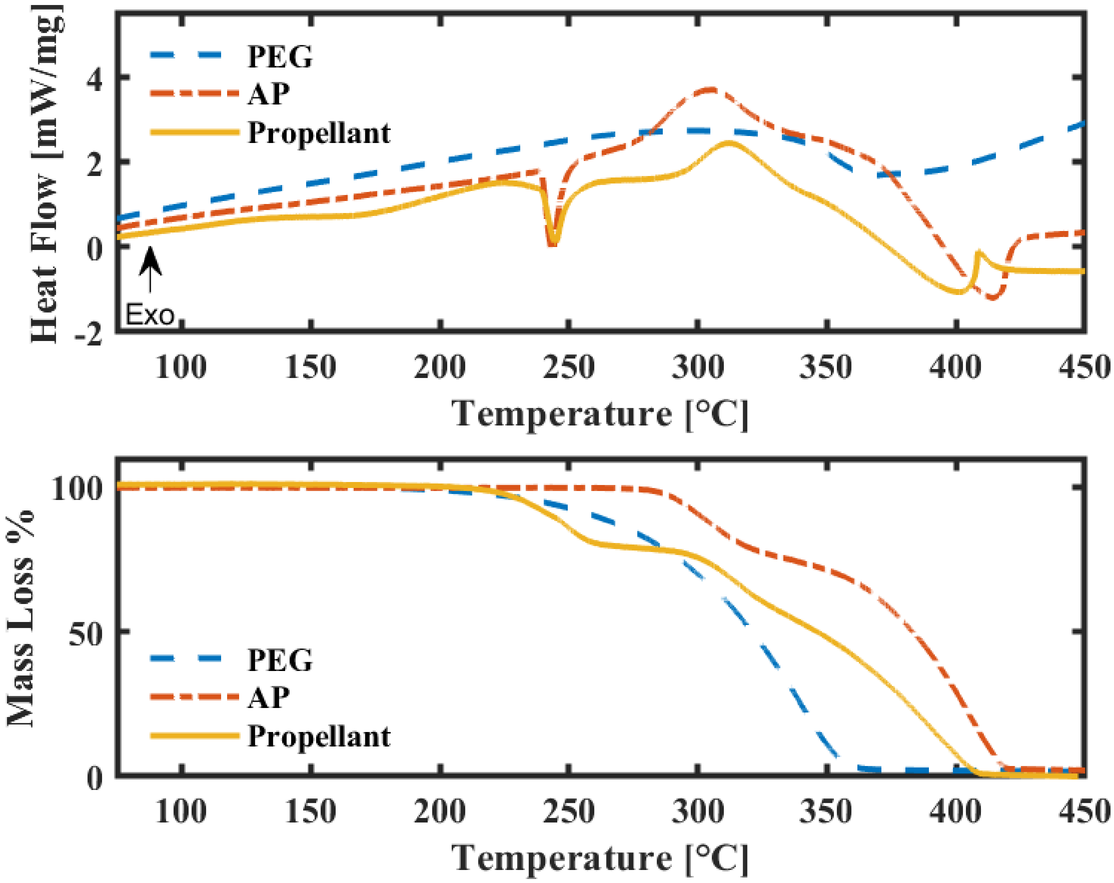

Figure 4.1: DSC and TG Analysis of PEG, AP, and Propellant

4.2 Materials Characterization

The results of the FTIR-ATR analysis conducted are shown in Fig. 4.2. The wavenumber associated with peaks in the absorbance indicates the type of bonds present, allowing for analysis of the complexation of the propellant. PEG is displays an O-H bond at 3450 cm^{-1}, a C-H bond at 2800 cm^{-1}, and a C-O bond at 1100 cm^{-1}. Likewise, AP presents an N-H bond at 3300 cm^{-1} and exhibits three peaks associated with Cl-O bonds due to its tetrahedral symmetry at 1400 cm^{-1}, 1100 cm^{-1}, and 600 cm^{-1}. In the propellant formulation, the C-O bond in the PEG, and the middle Cl-O bond in the AP, present at 1100 cm^{-1} and 1050 cm^{-1} respectively, merge into one peak at 1075 cm^{-1} as a result of the significant overlap between the C-O and Cl-O absorption bands. This suggests a possible interaction between these two functional groups. In addition, the N-H bond in the AP at 3300 cm^{-1} is red-shifted by 20-50 cm^{-1} in the propellant formulation. This confirms the complexation of AP with PEG, which allows the propellant to electrochemically decompose by weakening the C-O bond within the polymer [13].

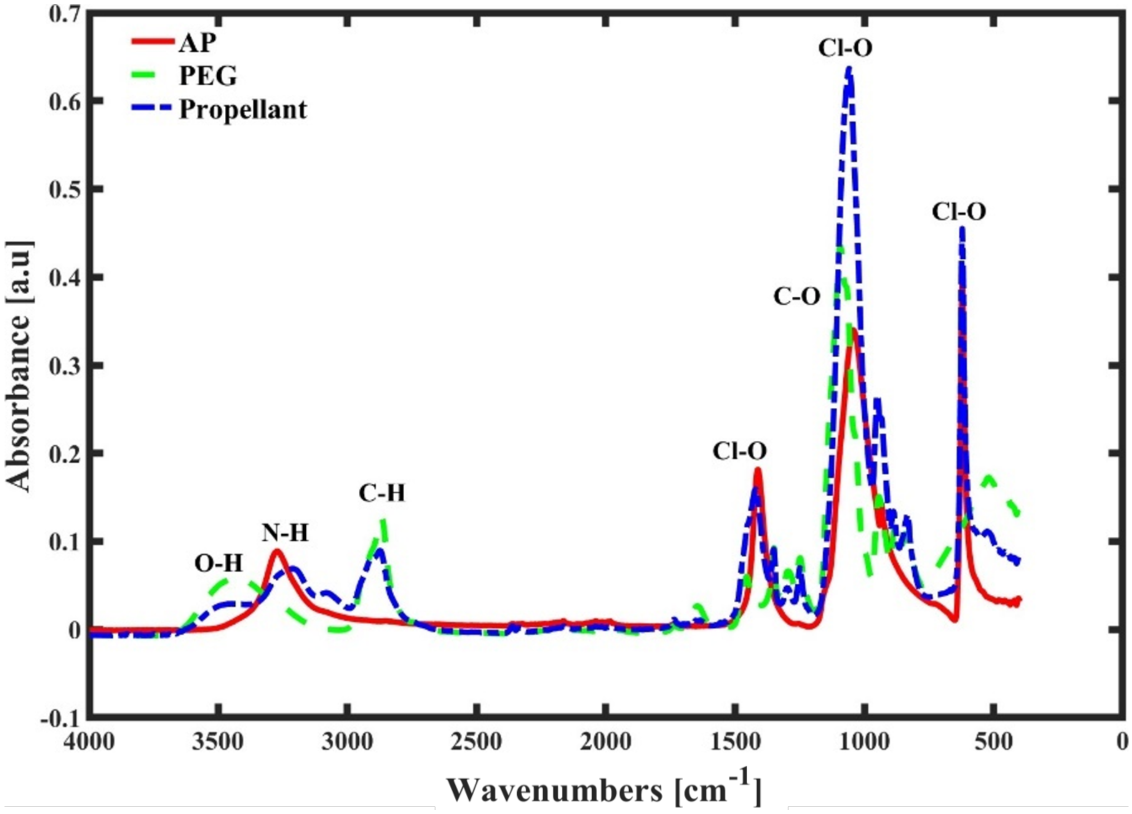

Figure 4.2: ATR Analysis of PEG, AP, and Propellant

4.2.1 Electric Field Simulations

Simulations of the electric fields through the test configurations with an applied voltage of 175 V are shown below in Figs. 4.3 and 4.4. The color map and scale bar indicate the magnitude of the electric field, and the arrows represent vectors in the direction of the electric field.

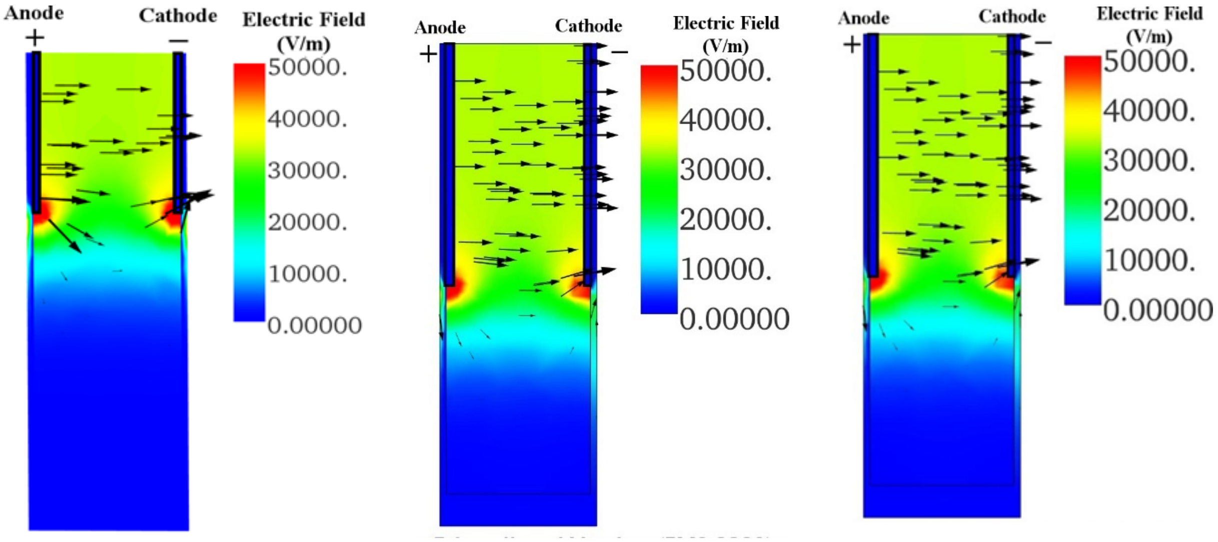

(a) 6.35 mm Electrodes (b) 9.53 mm Electrodes (c) 12.7 mm Electrodes

Figure 4.3: Parallel Configuration Electric Field Simulation: Even Length Electrodes

As shown in Fig. 4.3 the electric field across equal-length parallel electrodes is relatively uniform and, as expected, does not vary as a function of electrode surface area. The electric field in the uniform section between the two electrodes was roughly 3.2×10^4 V/m, with spikes up to 5×10^4 V/m at the bottom edges of the electrodes due to fringe effects [112]. Likewise, electric field simulation of the uneven electrode configurations (Fig. 4.4) produced a similar magnitude electric field as the parallel electrode configuration. The uniform section between both electrodes remains fairly constant at 2.3×10^4 V/m in both configurations. Further, there is a spike in field intensity surrounding the bottom edge of the shorter electrode, which roughly doubles the localized electric field in that region. In addition, there is a slight

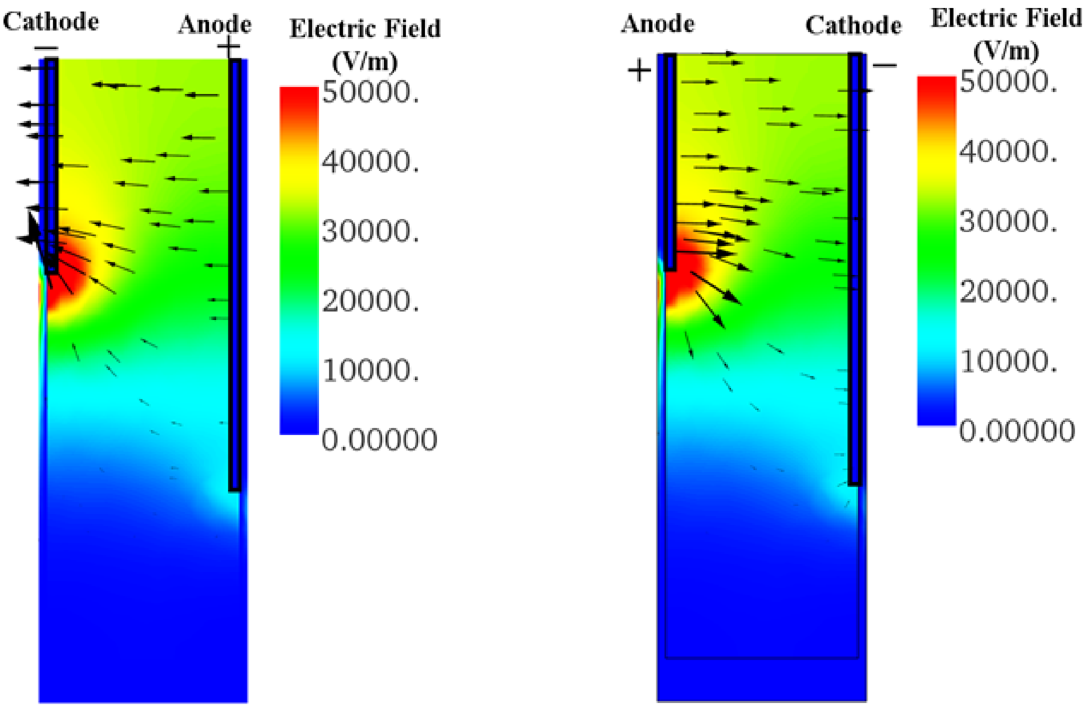

(a) Long Anode (b) Long Cathode

Figure 4.4: Parallel Configuration Electric Field Simulation: Uneven Electrode Lengths

magnitude increase near the boundary of the shorter electrode that is not present on the boundary near the longer electrode. This is likely due to current density impacts at that shorter electrode. Further, the increased electric field strength at the edge of the anode, particularly in the short anode cases, seems to have an impact on the ignition location.

Similar to the parallel configuration, a simulation of the electric field strength was conducted in the concentric electrode configuration. Evaluations were also conducted with an insulative-sleeved inner electrode to match the height of the propellant contact region. It was seen in the simulations that the sleeved electrode had minimal impact on the induced magnetic field, and the magnitude of the field between the electrodes remained unchanged. As displayed in Fig. 4.5 and Fig. 4.6, there is a peak around the top edge of the central electrode and the bottom edge of the outer ring electrode. These results are consistent with the comparable parallel configurations discussed above. In both cases the magnitude of the electric field is strongest along the top edge of the central electrode and at the bottom edge of the outer electrode. Further, in the region between the two electrodes, the electric field increases from 5×10^4 V/m at the outer electrode to 7×10^4 V/m at the inner electrode. Spikes at the bottom edge of the outer electrode are once again fringe effects likely due to a current density increase at the edge of the electrodes [112]. Further, the electric field visible in the body of the electrode holder is present due to the electric permittivity of the electrode holder. Despite this, there is no current through the holder due to the magnitude of the electric field remaining below the dielectric constant of the material. Fig. 4.7 depicts the electric field in the sleeved electrode case, where the bulk field strength between the electrodes is nearly identical to the unsleeved configuration at to 7×10^4 V/m at the edge of the inner electrode, but decreasing to 4×10^4 V/m at the outer electrode. In addition, there is a spike in bottom of the electrode holder, which was not present in the unsleeved variation. This is due to fringe effects and is not impact the system because the magnitude of the electric field in this region is below the dielectric constant of the electrode holder.

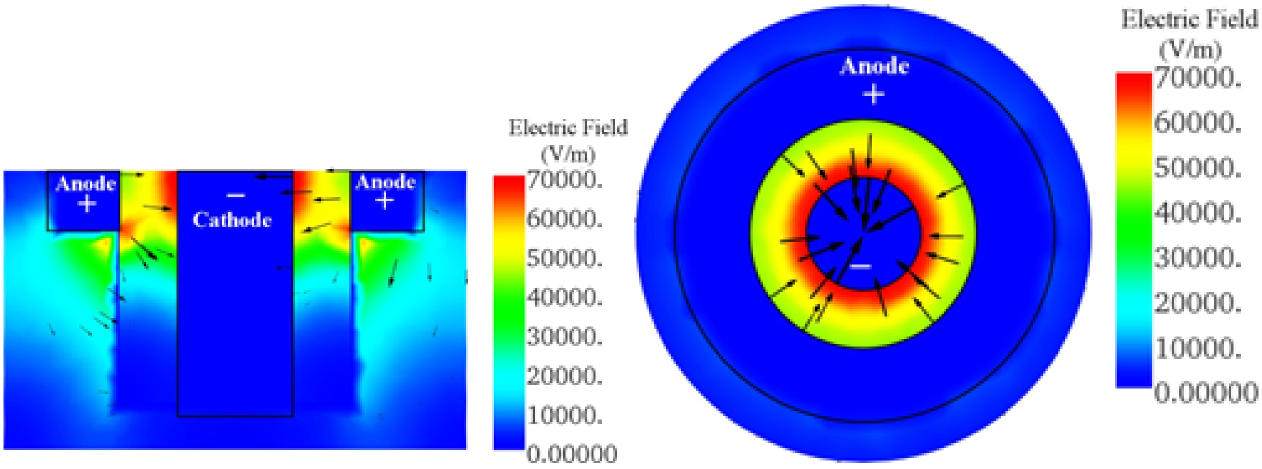

(a) Center Section View (b) Top View

Figure 4.5: Concentric Configuration Electric Field Simulation: Anode Out Configuration

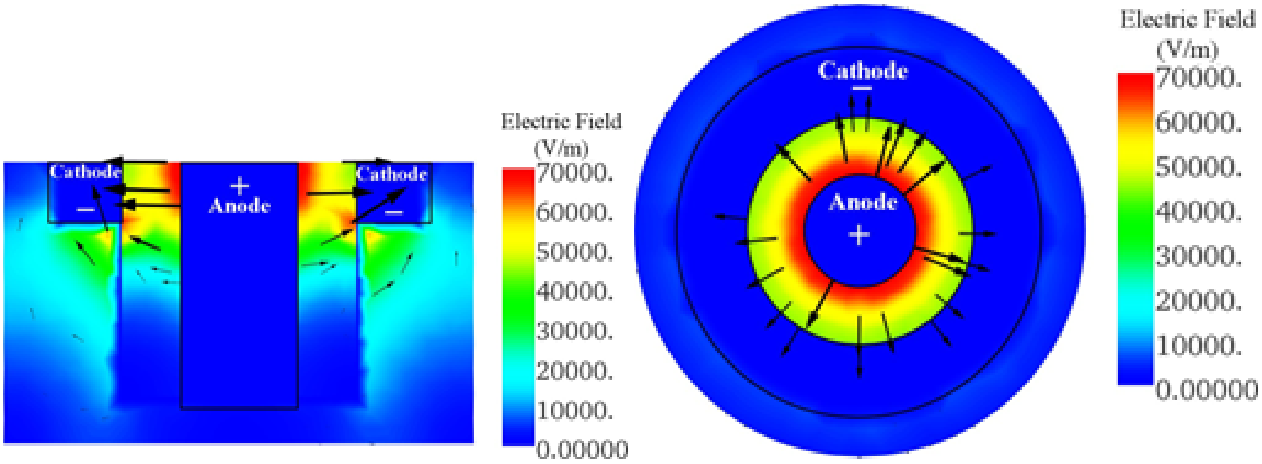

(a) Center Section View (b) Top View

Figure 4.6: Concentric Configuration Electric Field Simulation: Cathode Out Configuration

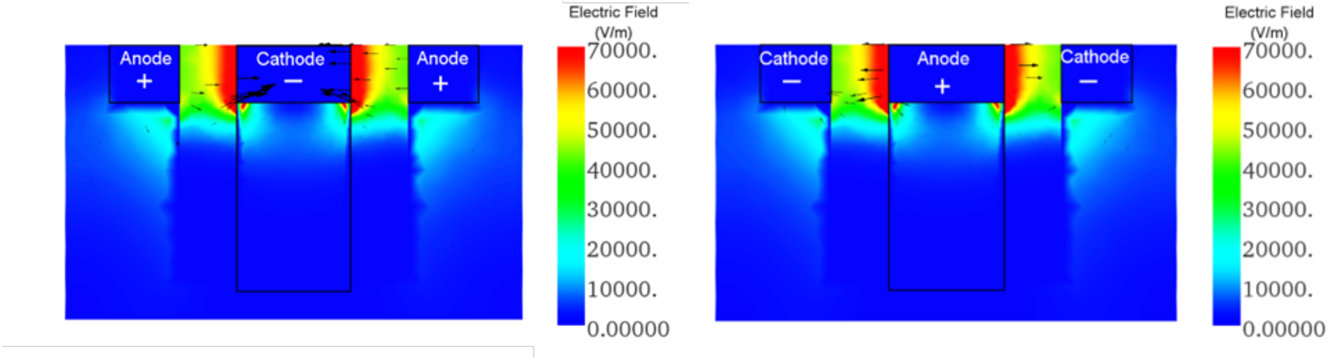

Figure 4.7: Section View of Electric Field Simulation Sleeved Electrode Configuration: Anode Out (Left) and Cathode Out (Right) Configurations

Chapter 5

Ignition Experiment Results

5.1 Propellant Formulation Screening

As indicated in Fig. 3.1, there is a performance benefit to increasing the concentration of AP relative to LP in the propellant; however, the use of AP as the sole oxidizer has not been previously reported on, leading us to explore a range of potential propellants. The goal was to find a formulation that is a gel that achieves sufficiently fast ignition and is self-propagating once power to the electrodes is turned off. Experiments were carried out in the parallel electrode configuration with 9.53 mm long electrodes. Ignition delay was determined through high-speed cinematography by synchronizing the camera with the power supply. In the high-speed footage, ignition was visually determined as the first light of the propellant. The first sampling varied the relative concentration of AP to LP in with a 25 wt% concentration of PEG. Indicated in ignition delay figures, starting with Fig. 5.1 where the points are the average ignition delay of each experiment at a given applied voltage. The error bars indicate the standard error (SE), where n is the number of samples and σ is the standard deviation of the population.

$$SE = \frac{\sigma}{\sqrt{n}} \tag{5.1}$$

It is noted in Fig. 5.1 that ignition delay time increases as the concentration of LP increases, from around 4 seconds with sole AP to over 30 seconds with solely LP. This further motivates the exclusion of LP in future propellants, as a fast response time is vital to thruster applications. Importantly, the formulation of only AP and PEG successfully ignited under an applied voltage, which is attributed to the complex that has been formed between the ammonium and the PEG. Due to these results, a further panel was conducted utilizing solely PEG and AP, this time varying the concentration of PEG captured in Fig. 5.2. The ignition delay at 30 wt% PEG was considerably slower than the 20 and 25 wt% PEG formulations, igniting at around 8 seconds compared to around 3 seconds. This is attributed to the higher wt% PEG formulation being under-oxidized with an equivalence ratio of 2.18, reducing the effectiveness of thermal decomposition due to PEG having a higher heat capacity than AP [113, 114]. Considering these results, formulations of 20 wt% and 25 wt% PEG, with AP as the sole oxidizer, were considered.

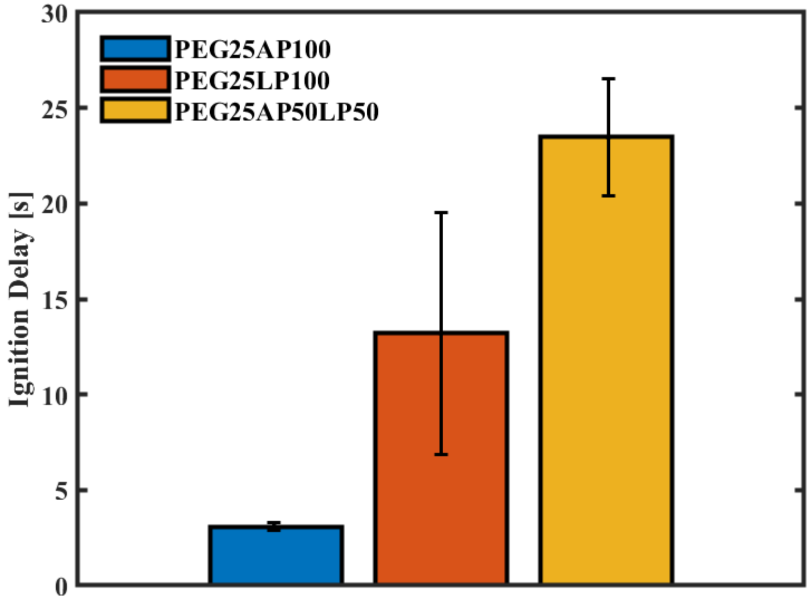

Figure 5.1: Ignition Delay of AP/LP Based Propellant at 150 V

The propagation of the 25 wt% PEG was intermittent due to it being near the upper prop-

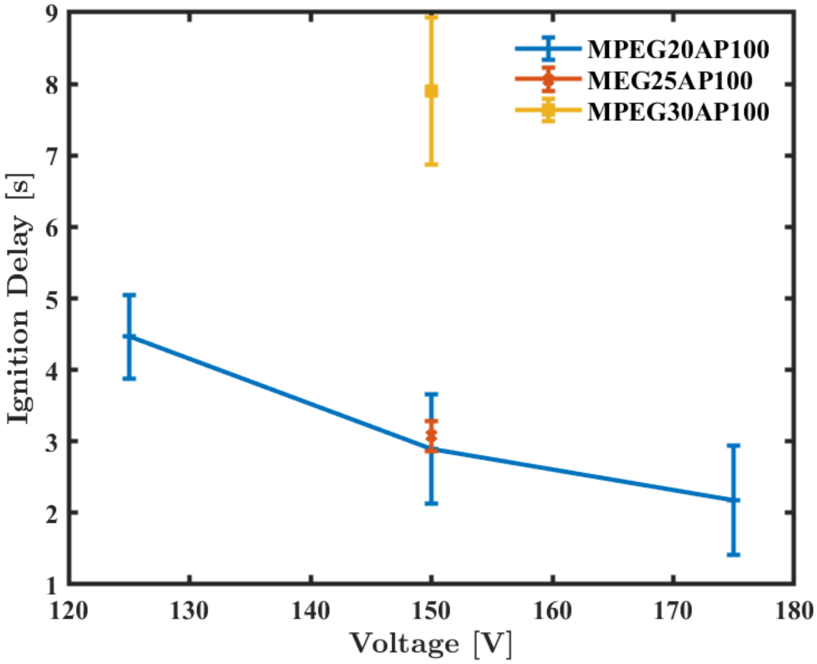

Figure 5.2: Ignition Delay of Variable PEG Concentrations in Binary PEG/AP Propellant

agation limit. Due to this a constant supply of electrical energy after ignition was required to continue burning of this propellant reliably. Regardless, a regression rate analysis was conducted between the two. To ensure consistency, only samples of the 25 wt% PEG that propagated freely were considered. Both formulations followed a linear regression profile after ignition, as indicated in Fig. 5.3, with the 20% PEG burning at nearly 0.2 mm/s faster rate than the 25% PEG formulation. This is attributed to the 20% fuel propellant being significantly closer to stoichiometric conditions. This leaves PEG20AP100 as the most favorable option, however, this formulation has a high viscosity and could be classified closer to a wet powder than a gel. With this in mind, a formulation with EG was created as an attempt to reduce the viscosity of the propellant by reducing the molecular weight of the fuel component compound. This follows the logic behind the use of PEO in solid formulations and PEG in gel formulations. The ensuing formulation of 20 wt% EG with AP marginally reduced the viscosity of the propellant, however, the performance was heavily impacted as shown in Fig. 5.4. This excluded EG from the study, as the rest of the experimentation was conducted with the PEG20AP100 formulation.

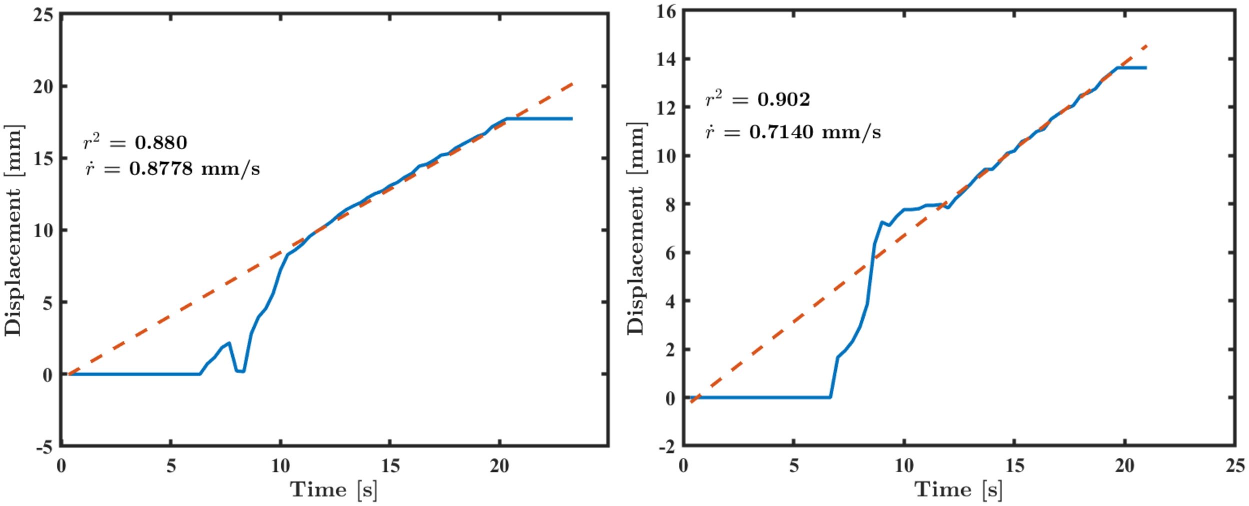

(a) PEG20AP100

(b) PEG25AP100

Figure 5.3: Regression Rate Comparison of PEG/AP Propellants

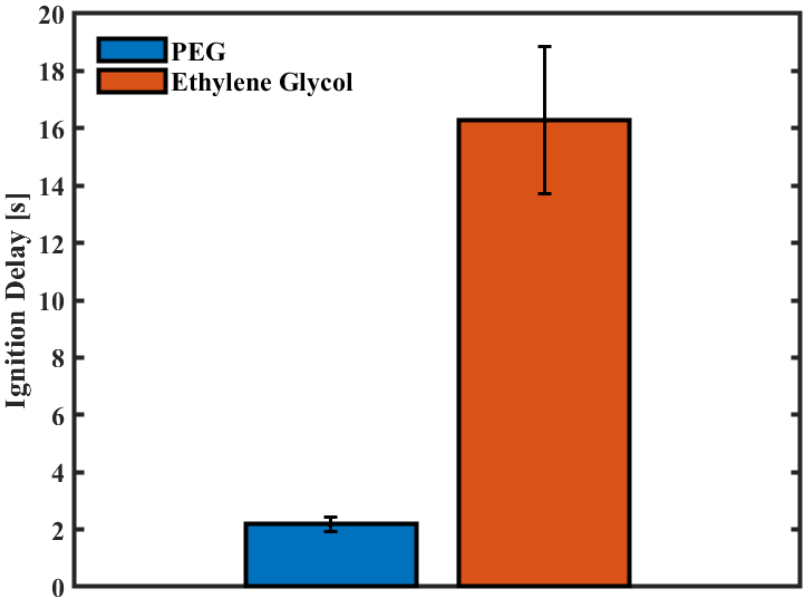

Figure 5.4: Ignition Delay of PEG and EG Based Propellants at 175 V

Further analysis of potential propellants turned to the particle size of the oxidizer, as experiments were conducted with 90 and 200 μm AP. Fig. 5.5 depicts the ignition delay difference between the two sizes, where it is noted that the smaller particle size offers lower ignition delays. At these high concentrations of oxidizers, the propellant is oversaturated, so the oxidizer particulate is still present in the mixture, and the smaller particles provide better combustion characteristics as the surface area to volume ratio is larger.

AP supply issues led us to source AP from multiple manufacturers, and as such, the performance of each manufacturer differed. This is likely due to different anti-caking agents utilized in the storage and drying process of manufactured AP. Regardless, all further experimentation was conducted with 90 μm AP in the 20 wt% formulation with AP supplied by Firefox Enterprises.

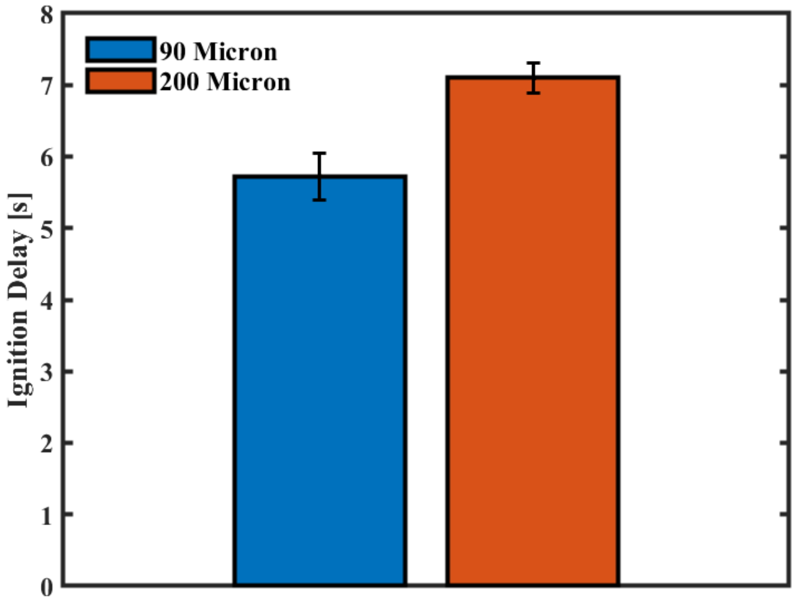

Figure 5.5: Ignition Delay Comparison between AP Particle Sizes at 175 V

5.2 Parallel Electrode Configuration Ignition

5.2.1 Ignition Delay

For the even and long cathode electrode configurations, at all applied voltages, ignition occurred at the anode. On the other hand, with a long anode ignition always occurred at the anode at the lowest voltage we probed, but as voltage increased the location of ignition varied with some at the anode and some at the cathode. In most cases, ignition occurred near the surface of the propellant on the anode side as displayed in Fig. 5.6. Ignition is indicated by the presence of a blue flame at the surface of the propellant near the anode. However, in some experiments with the shorter anode, ignition occurred near the bottom edge of the anode (Fig. 5.7), at a significantly higher rate as opposed to near the surface of the propellant. This may in part be due to the high viscosity of the propellant restricting decomposition products from escaping, and the larger electric field magnitude at the edge of the shorter anode, causing a buildup of oxygen, leading to ignition. Experiments that resulted in subsurface ignition were not included in the results presented since they were not representative of the overwhelming majority of experiments and only occurred in one electrode configuration.

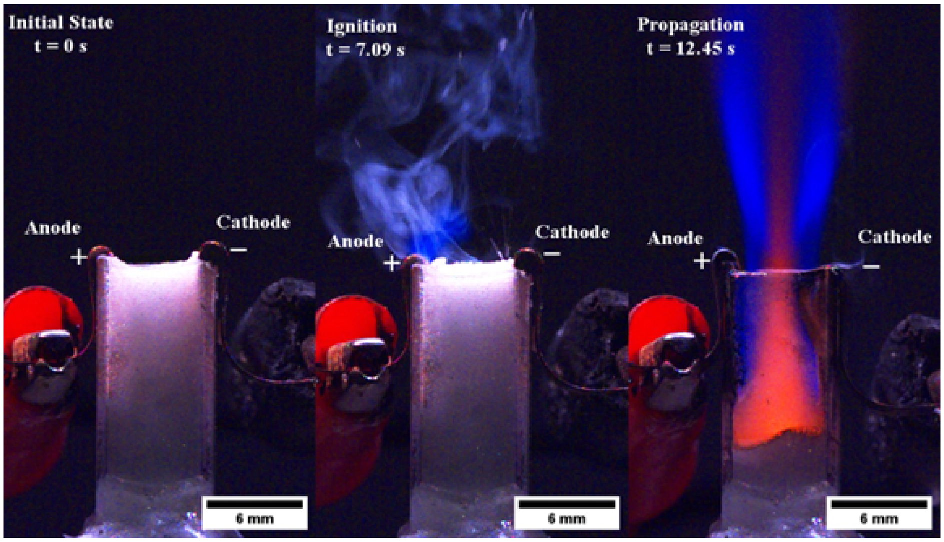

Figure 5.6: Ignition at Propellant Surface of Anode

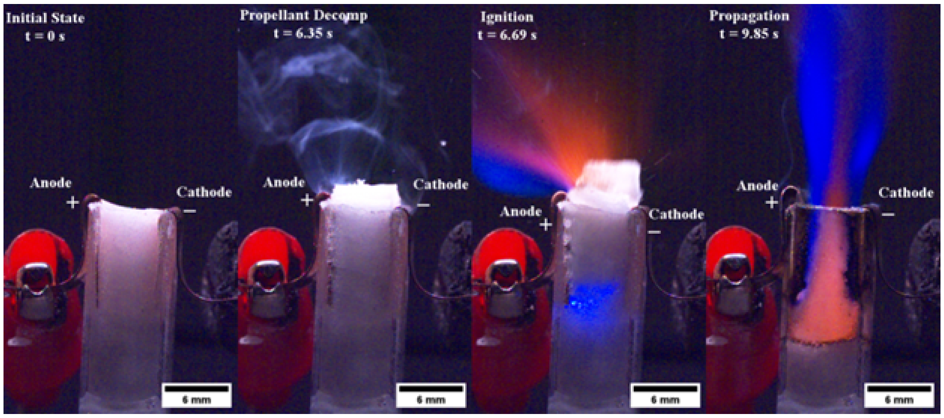

Figure 5.7: Ignition within Propellant Volume at Bottom of Anode

Different electrode lengths were examined to help understand the dependence on electrode surface area. When both anode and cathode were the same length, for a fixed input voltage, the effect of increasing electrode length decreased the ignition delay, which can be seen in Fig. 5.8. Doubling the length of the electrodes resulted in a reduction of ignition delay by about ½. Fig. 5.9 depicts the ignition delay as a function of applied voltage for conditions of even length electrodes and for variations in which one electrode was longer than the other. For electrodes of even length, the ignition delay decreases approximately linearly with increasing voltage.

Implementing an uneven electrode configuration increased the ignition delay at all voltages compared to the even configuration. Interestingly, the linear relationship between voltage and ignition delay in the even length experiments is no longer observed with either polarity. The long cathode configuration maintains a decreasing ignition delay with increasing voltage, but it no longer appears linear and in the extreme case at the lowest voltage probed exhibits an ignition delay of about 2.5 times that of the even electrode configuration. In fact, the long cathode arrangement resulted in the longest ignition delay of all of the configurations at the lowest, but as voltage is increased, the ignition delay becomes shorter than that of the long anode configuration. On the other hand, the long anode configuration exhibits an increasing ignition delay from 150 to 175 V, but from 175 to 200 V, the ignition delay decreased again as would be expected based on all of the other results.

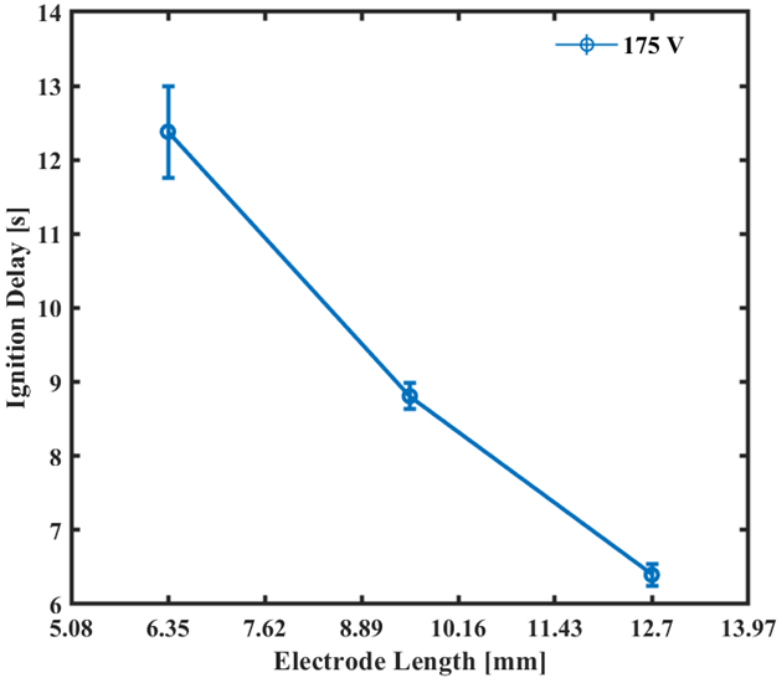

Figure 5.8: Parallel Ignition Delay: Even Length Electrodes

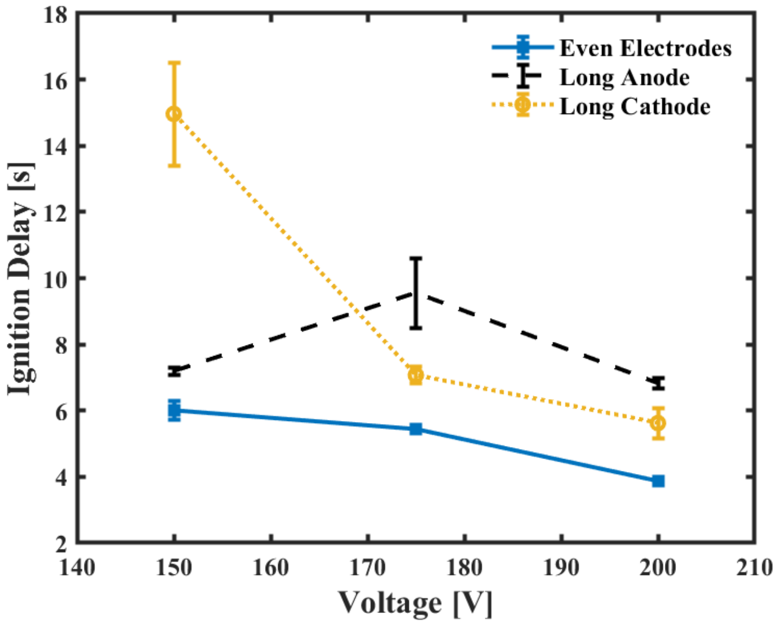

Figure 5.9: Parallel Ignition Delay: Uneven Electrode Lengths

5.2.2 Current Analysis

Current was collected in each experiment and the current peak was observed to correspond closely to the ignition delay in the parallel electrode cases, as depicted in Fig. 5.10, which displays the current traces for the even length electrode configurations up to their respective peaks where the vertical lines indicate ignition. Notably, the peak current decreases with decreasing electrode length. Similarly, Fig. 5.11 shows the current traces for the uneven electrode configurations. In the long cathode experiments, which experienced a faster ignition delay than the long anode configuration, except at the lowest voltage, the current at ignition is highest for the highest voltage and decreases with decreasing voltage. Conversely, with the long anode configuration, the ignition current was essentially constant ($\backsim$ 0.4 A) regardless of the applied voltage, while the ignition delay increased with decreasing voltage. Table 5.1 further exemplifies the differences in current between the long cathode and long anode configurations. In either electrode configuration, ignition delays closely correspond to peak current as at a constant voltage this current peak corresponds to the lowest resistance and highest conductivity of the propellant. Ion transport increases with conductivity, allowing for an increased rate of decomposition leading up to ignition.

Table 5.1: Propellant Properties at Peak Current

Long Cathode			**Long Anode**		
Voltage [V]	Current [A]	Resistance [Ω]	Voltage [V]	Current [A]	Resistance [Ω]
150	0.27	552	150	0.43	346
175	0.5	354	175	0.37	474
200	0.61	327	200	0.42	471

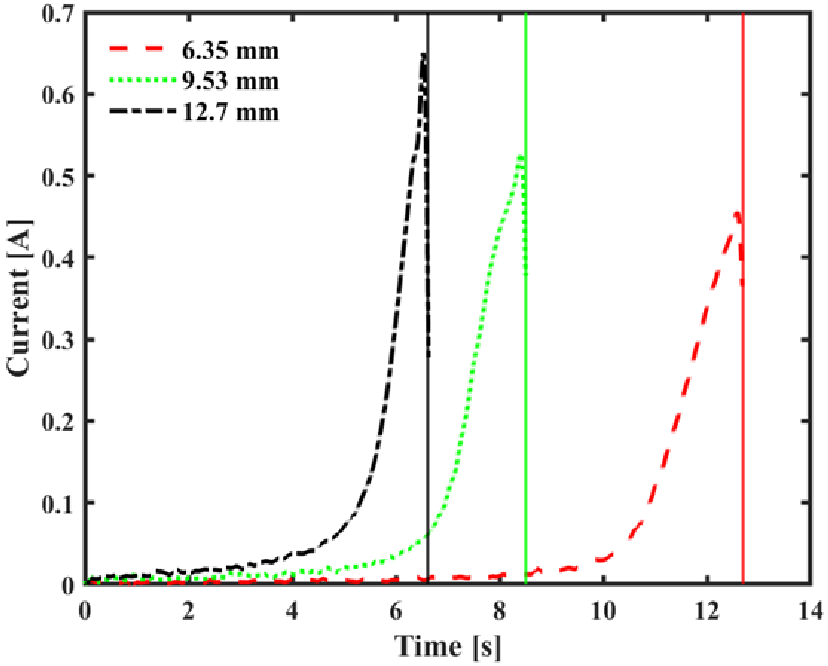

Figure 5.10: Parallel Even Length Electrode Current Traces: Vertical Lines Indicate Ignition

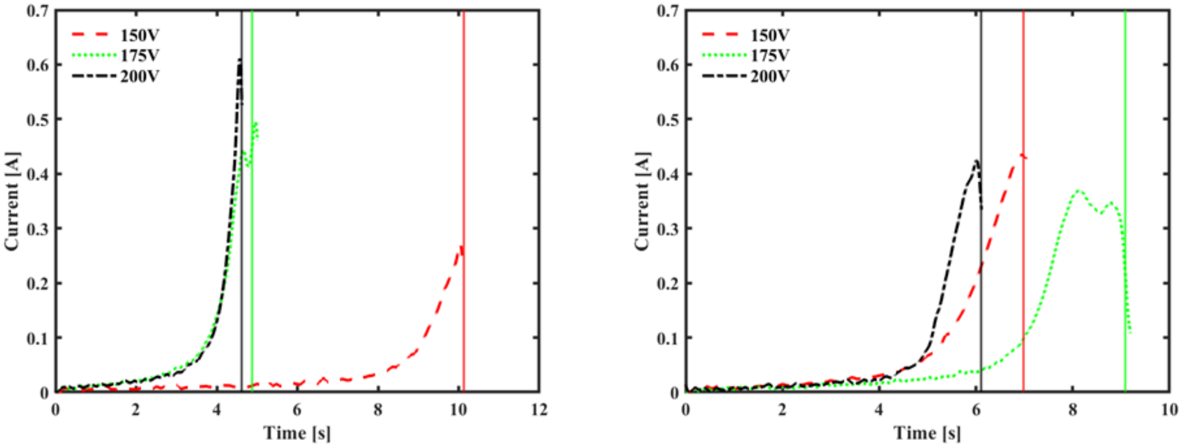

(a) Long Cathode (b) Long Anode

Figure 5.11: Parallel Uneven Electrode Current Traces: Vertical Lines Indicate Ignition

5.2.3 Thermal Camera Analysis

The FLIR X6983 thermal camera was utilized to gather a temporal profile of the surface temperature of the propellant and the electrodes leading up to ignition. A temperature range of 40 °C to 350 °C was utilized, and the camera was oriented in such a way so that there was a direct line of sight to the surface of the propellant and the top of each electrode with no interference from the test tube. The temperature-time history of the surface of the propellant and the surface of the electrodes in the even length electrode configuration is shown in Fig. 5.12. The temperature profiles are gathered by creating a point region of interest in the FLIR software at the edge of each electrode and the centerline surface of the propellant to obtain temporally resolved temperature at each location. As seen in Fig. 5.12, the propellant surface is initially heated linearly by Joule heating due to the resistivity of the propellant, which is present through the duration of the experiment. Lagging by 0.4 and 0.6 seconds is heat at the surface of the cathode and anode, respectively, which is comparable to results seen by Autry et al. [115] in their characterization of gel propellants. However, the opposite was observed by Gobin et al. [116] where the near surface of the anode appeared to heat before the cathode with their solid propellants. This may be expected considering differences in heating and ion mobility comparing a liquid to a gel to a solid. The exponential temperature increase in the electrodes above values observed in the propellant indicates that there is an electrochemical decomposition of the propellant occurring locally, very near the electrode surface.

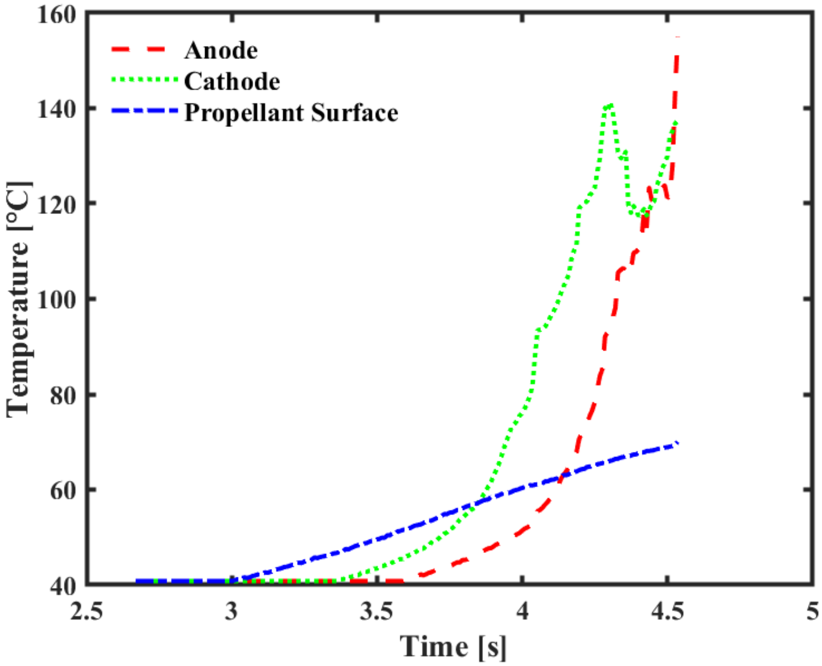

Figure 5.12: Temporal Temperature Trace up to Ignition

In considering the overall ignition process of the experiments discussed thus far, there are some important things to note. In all of our experiments, decomposition initially occurred at the cathode, while ignition always occurred at the anode other than in the long anode configuration at high voltage. To help explain this, consideration of the processes occurring at each electrode must be approached. The propellant was formulated with the intention of taking advantage of ion migration via a polymer electrolyte which begins with the formation of a complex between the salt and the polymer. The complexation of AP with PEG begins with the dissolution of AP into its anion and cation as shown in Equation 5.2. Once dissolved, a coordination polymer complex is formed between the PEG and the NH_4^+ ions present in AP. It is noted that these complexes are typically formed with a metallic ion [66], however, from a chemical standpoint, ammonium ions behave similarly to an alkali metal ion [117]. This complex allows for ionic transport under an applied voltage where ammonium ions move toward the cathode where they are reduced, as shown in Equations. 5.3 and 5.4. Likewise, the perchlorate ions move towards the anode, where they are oxidized and lose an electron as seen in Equations 5.5 and 5.6. This ion transport and interaction with the electrodes enables electrochemical decomposition over a purely thermal decomposition.

$$NH_4ClO_4 \rightarrow NH_4^+(aq) + ClO_4^-(aq) \tag{5.2}$$

$$3NH_4^+ + 3e^- \rightarrow 3/2H_2 + 3NH_3 \tag{5.3}$$

$$2H^+ + 2e^- \rightarrow H_2 \tag{5.4}$$

$$ClO_4^- \rightarrow 1/2Cl_2 + 2O_2 + e^- \tag{5.5}$$

$$ClO_4^- \rightarrow ClO_2 + O_2 + e^- \tag{5.6}$$

At the cathode, decomposition was noted with the formation of bubbles and gas evolution, presumably hydrogen and ammonia, as shown in Fig. 5.13. The images shown in Fig. 5.13 were collected with a propellant containing 25 wt% PEG in order to highlight this behavior, although it was also observable in the 20 wt% PEG propellant. Kim et al. found that the decomposition at the cathode is due to an instability in the PEG under an applied voltage with a variety of electrode materials, including copper [118, 119]. This is further supported by the thermal camera imaging and Fig. 5.12 which indicates a temperature rise occurring at the cathode before the anode. Meanwhile, at the anode, gaseous oxygen is generated, which appears to be a prerequisite for the ignition of this propellant.

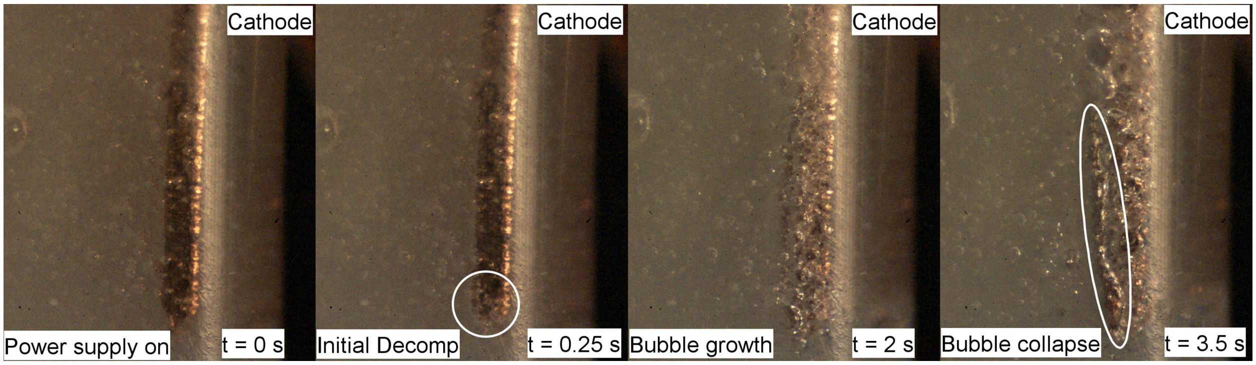

Figure 5.13: Sequence of Decomposition and Gas Generation Along Bottom Edge of Cathode

Considering the ignition behavior with the different electrode configurations highlights some important processes. As Fig. 5.10 shows, with even length electrodes, increasing the length of the electrodes results in a significant decrease in ignition delay. The electric field simulations verified that the strength of the field was not altered, thus, we can conclude that the longer electrodes provide additional surface area for electrochemistry to take place leading to faster ignition as both more gaseous fuel and oxidizer are formed. Further, current is an indicator of conductivity and reaction rate [120]. The larger electrodes provide additional surface area and therefore a greater number of reaction sites. This allows them to support a higher current than the smaller electrodes, indicating a greater reaction rate. Next, we consider the case of uneven electrodes which demonstrated wildly different ignition delay behavior compared to the even electrode configuration. The electric field simulations indicated significant differences from the even electrode case, specifically a lower bulk field strength and a strong field concentration at the lower corner of the shorter electrode. The difference in the electric fields, however, cannot explain the differences observed. For example, at the lowest voltage the ignition delay for the long cathode configuration is about 150% longer than that of the even electrode, while being only about 45% longer at the highest voltage. Meanwhile, in the case of the long anode, the ignition delay first increases with increasing voltage before decreasing again. Additionally, while using a long cathode we observed that the peak current increases with increasing voltage, but for the long anode, the peak current was approximately the same for all voltages. The effect of using one long electrode along with a shorter electrode is to limit the process taking place at the shorter electrode due to the requirement that any electrons lost during oxidation must be balanced by any gain of electrons during reduction. Therefore, by altering charge transfer, one can manipulate the processes taking place. Allowing one electrode to be longer than the other forces the process at the smaller electrode to be the limiting process. The long cathode thus restricts oxidation, resulting in a prolonged ignition delay at the lowest voltage and as voltage is increased, current is increased, resulting in faster reaction rates promoting faster ignition. Formation of gaseous oxygen has already been determined as a prerequisite for ignition and therefore the long anode results in a relatively fast ignition delay at the lowest voltage, where reduction is limited. This may in part be explained by the role of ion mobility. The perchlorate ionic radii is approximately 60% larger than that of the ammonium ion, so it is expected to be less mobile. As the voltage is increased, ion transport is promoted, which should reduce ignition delay, however we observed an increase in ignition delay with minimal change in current, seemingly making the propellant more resistive. The resistance may be increased by bubble formation and gas generation, which reduces contact between the electrode and electrolyte. Increasing the voltage further while the current again remains constant enhances joule heating, promoting a thermally driven ignition as local temperatures can be expected to be higher. This behavior is supported by probing the regions near the electrodes with the thermal camera. Images of the entire surface were collected and then probe lines parallel to the electrodes were constructed spanning the entire sample, working from the anode across to the cathode. Along each probe line an average temperature was computed, creating a temperature profile spanning the surface of the propellant. A representative profile of the average temperature across the propellant surface just prior to ignition for the long cathode case (Fig. 5.14) shows that the temperature near the anode is considerably higher than that of the cathode while the bulk of the propellant is at a relatively constant temperature. This general behavior was consistent for all long cathode experiments. On the other hand, the temperature profiles for the long anode case change dramatically as voltage is increased (Fig. 5.15). At the lower voltage the highest temperatures occur at both the anode and cathode, indicating fairly even electrolytic decomposition at both electrodes. As the voltage is increased, the high temperature shifts to the cathode, which limits the reduction of ions, and generates higher temperatures.

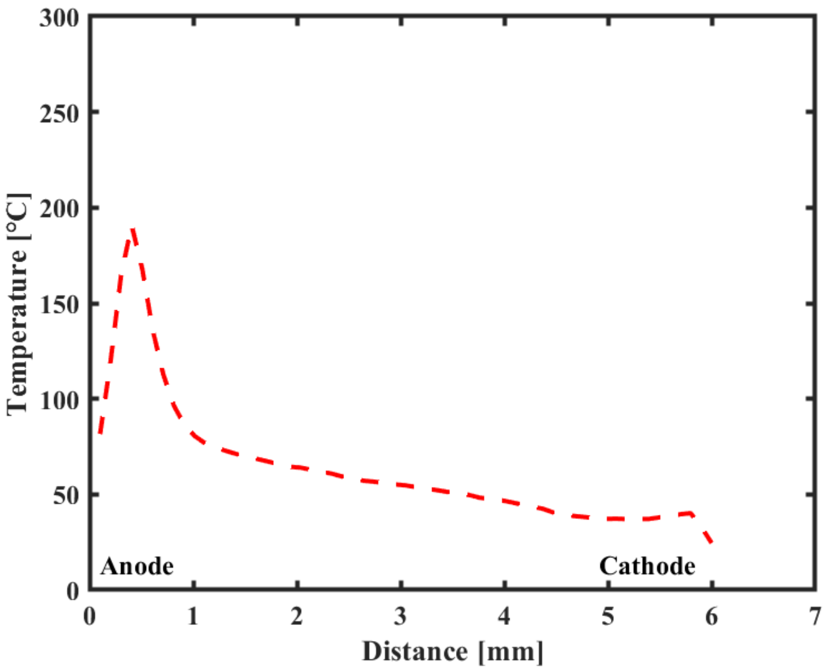

Figure 5.14: Long Cathode 200V: Spatially Resolved Temperature Profile

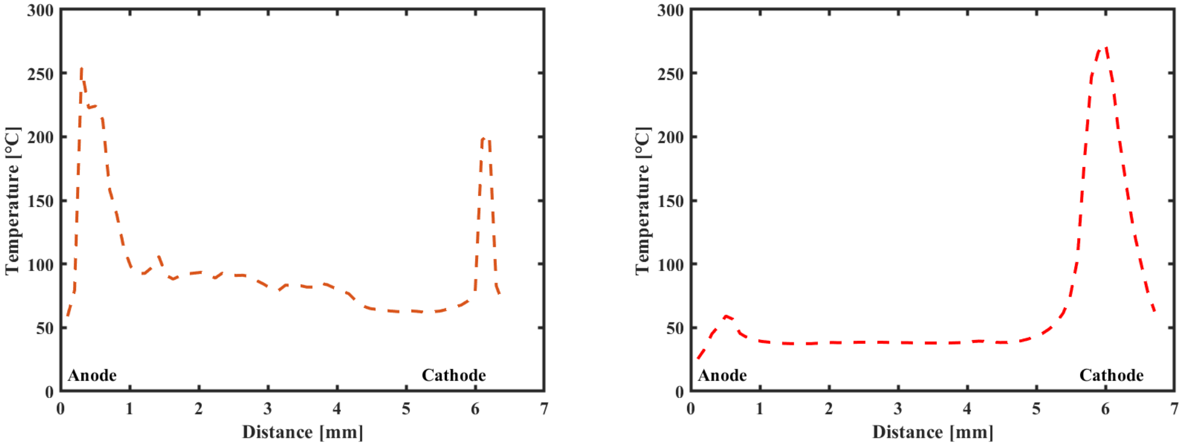

Figure 5.15: Long Anode 150 V (Left) and Long Anode 200 V (Right) Spatially Resolved Temperature Profile

5.3 Concentric Configuration Ignition

5.3.1 Ignition Delay

Similar to the parallel electrode configuration, ignition delay experiments were conducted with a concentric electrode configuration. The electrode surface areas of each electrode are shown in Table 5.2, where the electrode surface area is defined as the area in contact with the propellant. In the concentric configuration, the radial distance separating electrodes was 3.18 mm, and thus a baseline test was conducted in the parallel configuration with an applied voltage of 175 V to use as a comparator, which resulted in an ignition delay marginally less than 2 seconds. Initial experimentation observed both 25 wt% and 20 wt% PEG; however, to maintain consistency between this test campaign and the parallel electrode test campaign, the majority of the results were conducted with 20 wt% PEG. Nonetheless, results in Fig. 5.16 and 5.17 depict similar trends where the cathode out configurations experienced generally lower ignition delay times than the anode out configuration. In addition, the magnitude of the applied voltage appears to impact PEG25AP100 greatly, with ignition delay times increasing at lower voltages more so than PEG20AP100. However, the significantly longer ignition delays at lower voltages in Fig. 5.16 potentially suggest a greater influence due to electrochemistry rather than thermal mechanisms. Akin to the parallel configuration, all further experimentation was conducted with the 20 wt% formulation with AP supplied from Firefox.

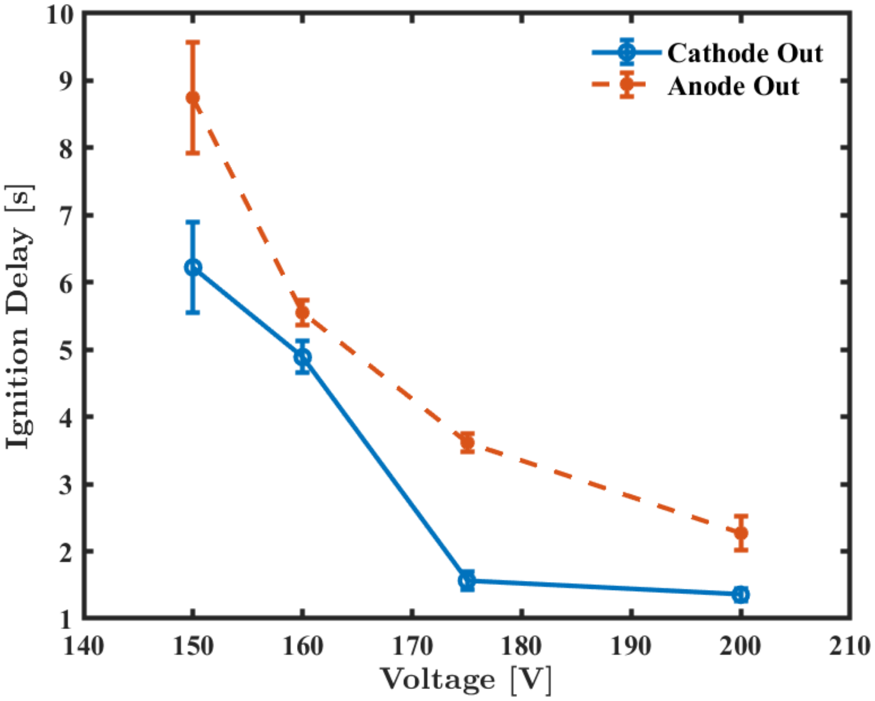

Figure 5.16: Concentric Ignition Delay 25 wt% PEG

As shown in Fig. 5.17, ignition delays showed relative consistency between the anode out and cathode out polarities, where the propellant ignited in about 2 seconds in all cases and was relatively insensitive to the magnitude of voltage applied. These ignition delays compare closely to the baseline parallel electrode case (3.18 mm separation). To isolate electric field impacts from surface area impacts, an insulating sleeve was introduced on the inner rod electrode. The sleeve matched the height of the inner rod electrode to the height of the outer ring electrode and scaled the surface areas accordingly, as shown in Table 5.2. In both cases, the magnitude of the electric field is unaffected so that the only change between the sleeved and unsleeved configurations is the electrode surface area. Reducing the total surface area of the electrodes by introducing the sleeve increased ignition delay times in both polarities, indicating a strong dependence on the surface area of the electrode. Further, the sleeved, anode out case exhibited the longest ignition delay times and is the most sensitive to the magnitude of the applied voltage.

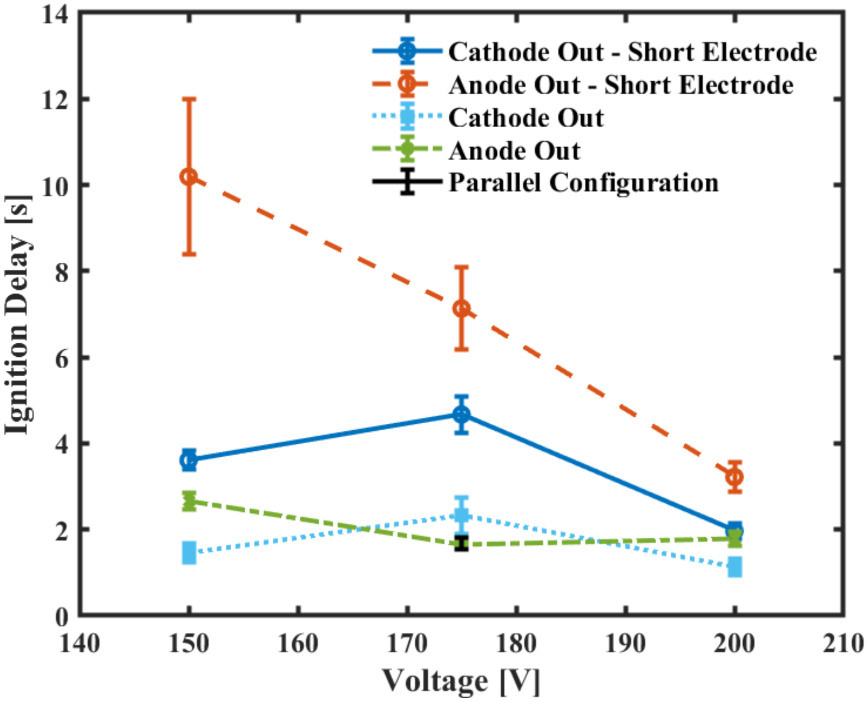

Figure 5.17: Concentric Ignition Delay 20 wt% PEG

Table 5.2: Concentric Electrode Surface Area

Concentric Electrode Configuration	Propellant Contact Area [mm^2]
Outer (Ring)	126
Inner Rod (Full Length)	253
Inner Rod (Sleeved)	63

5.3.2 Current Analysis

Unlike the parallel electrode configuration, ignition occurred substantially before the current peak for the concentric electrode configuration as depicted in Fig. 5.18, where the vertical lines indicate ignition. This observation was consistent across voltages and polarities. As applied voltage is increased the anode out configuration sees an increase in maximum current draw, whereas in the cathode out case the peak current is roughly the same ($\backsim$ 0.5A) across all voltages. These peak current trends are consistent between the reduction and oxidation limited configurations in both parallel and concentric experiments. The anode out, and long cathode cases are oxidation limited due to the smaller surface area of the anode, and here the current increased, and the ignition delay slightly decreased with increased voltage. On the other hand, reduction is limited in the cathode out and long anode configurations, where the current traces for both remain relatively constant across the range of voltages. From 150 V to 175 V the ignition delay slightly increases, which is likely due to the formation of bubbles and gas generation at the electrode electrolyte interface. As the voltage increases further, the resistance of the propellant is increased, which promotes further Joule heating leading to higher temperatures and shorter ignition delays. The sleeved electrode cases depict similar behavior with an oxidation or reduction limited half reaction, yet the analysis is not as consistent with the unsleeved variations. In these experiments, there was no appreciable trend between the current (Fig. 5.19) and ignition delay characteristics; however, as noted, the ignition delay increased in all cases compared to the unsleeved variations. This is likely due to the reduced overall surface area of the electrodes, despite the ratio between the surface area of the anode to cathode remaining the same. A likely explanation is in the difference in the electric field between the configurations, where the bulk field strength remains the same, however the strong concentration on the lower edge of the ring electrode seen in Fig 4.5 and Fig. 4.6, is not present in the sleeved electrode cases in Fig. 4.7.

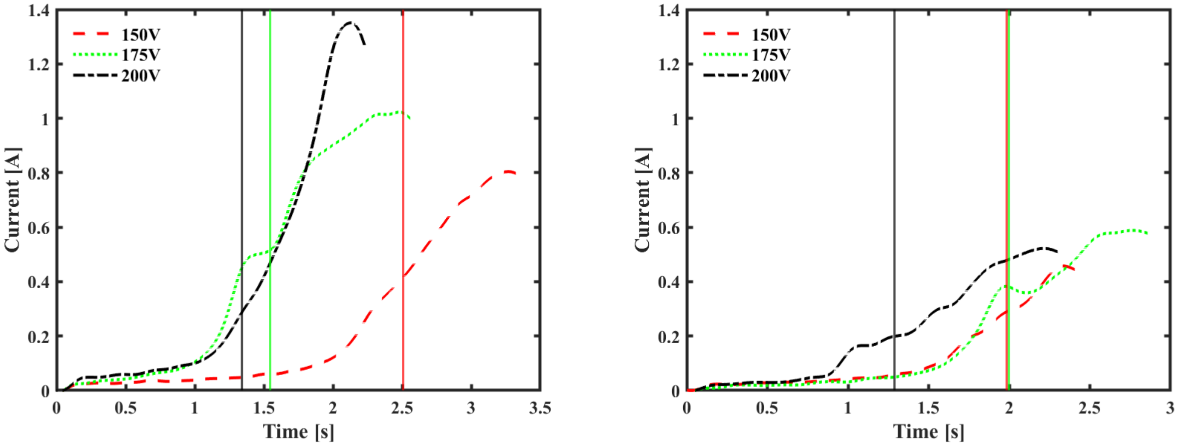

(a) Concentric Configuration: Anode Out

(b) Concentric Configuration: Cathode Out

Figure 5.18: Concentric Current Traces: Vertical Lines Indicate Ignition

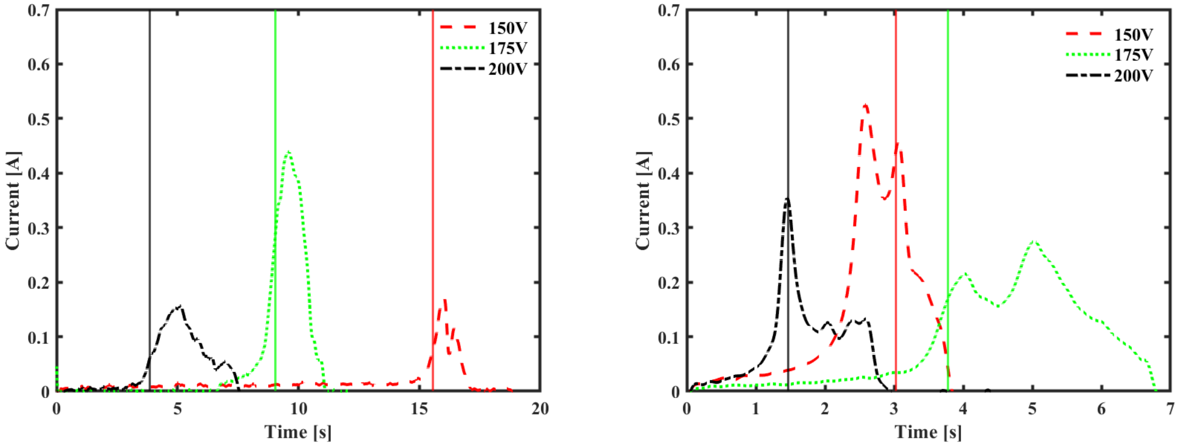

(a) Anode Out Sleeved Electrode

(b) Cathode Out Sleeved Electrode

Figure 5.19: Concentric Current Traces (Sleeved Electrode): Vertical Lines Indicate Ignition

5.3.3 Thermal Camera Analysis

Analogous to the thermal results from the parallel configuration, experiments were conducted in the concentric configuration to determine the nature of the initial decomposition. Initial decomposition location is qualitatively defined at the location of initial heating, shown in Fig. 5.20 and Fig. 5.21. Unlike the parallel configuration, the electrodes showed no evidence of heating, most likely due to the large thermal mass of the electrodes compared to the thinner parallel electrodes. Initial heat generation in the propellant originated from the inner electrode, regardless of polarity or configuration, indicating a strong dependence on the electric field as the magnitude of the electric field is strongest around the surface of the inner electrode. Despite the initial heat generation occurring at the inner electrode, the spatially resolved thermal profile at 175V for the sleeved electrode configuration, the moment before ignition indicates a strong dependence on the electrode surface areas, as shown in Fig. 5.22. In the anode out sleeved polarity, reduction is limited due to the cathode being small. This leads to a higher temperature at this location, consistent with observations made in the parallel case. On the contrary, the cathode out sleeved polarity provides an oxidation limited reaction, and the temperature leading up to ignition is greater at this interface. As indicated in the parallel electrode experiments, the limiting electrode dictated the temperature evolution of the propellant, due to the restricted electrochemistry occurring at the electrode with a smaller contact area.

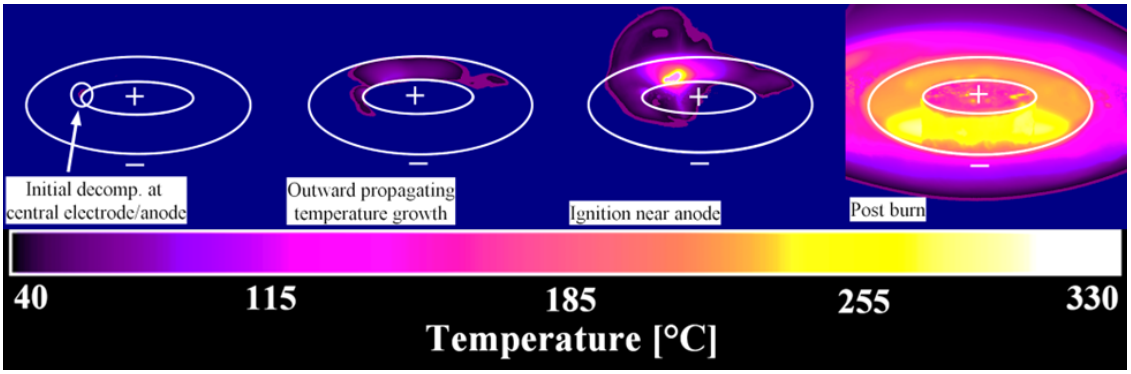

Figure 5.20: Thermal Camera Ignition Sequence: Cathode Out Configuration

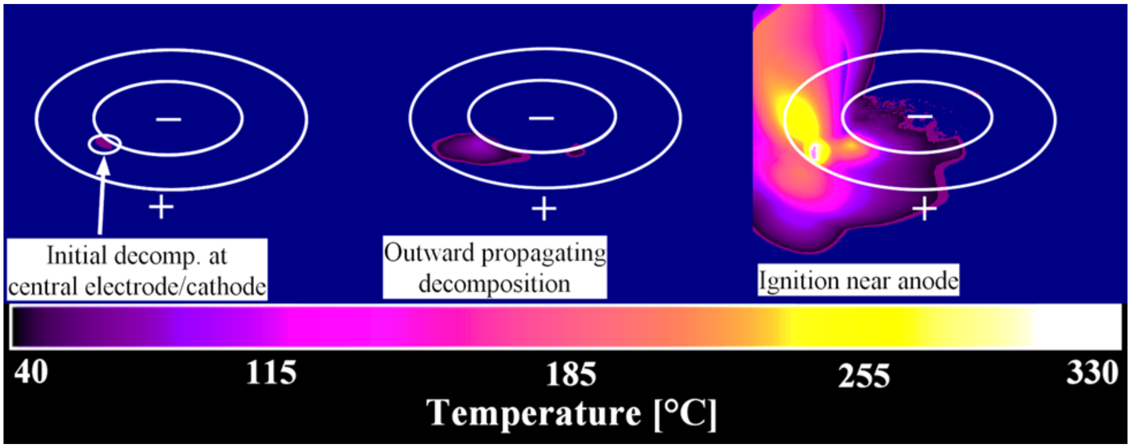

Figure 5.21: Thermal Camera Ignition Sequence: Anode Out Configuration

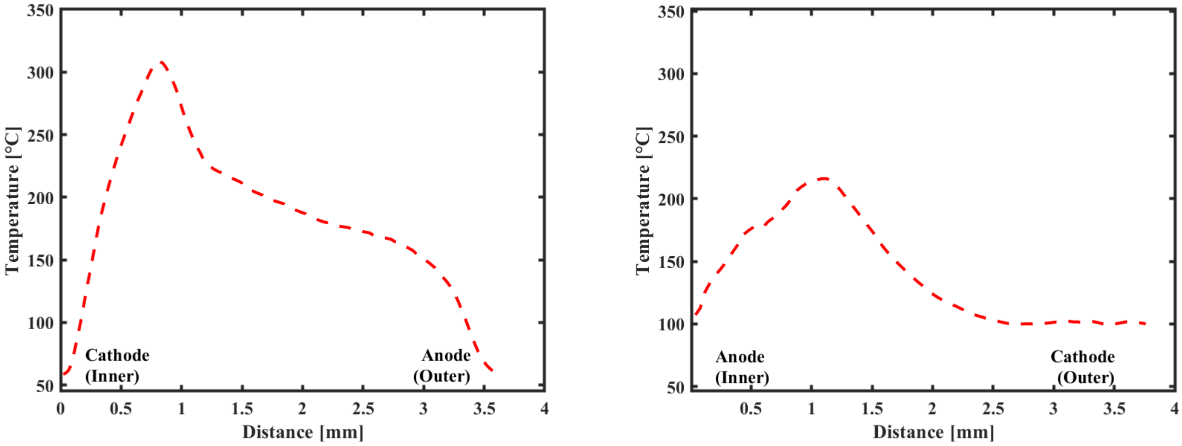

(a) Anode Out Sleeved Electrode

(b) Cathode Out Sleeved Electrode

Figure 5.22: Concentric Sleeved Electrode Spatially Resolved Temperature Profiles

Chapter 6

Conclusions

6.1 Electrically Controlled Ignition Experiments

The formulation of an electrically initiated propellant utilizing PEG and AP as the sole oxidizer was experimented on, characterizing decomposition and ignition mechanisms. The composition of the propellant is derived from a polymer electrolyte, in which an ionically conductive material, in this case AP, is complexed with a low molecular weight PEG This complex was verified through ATR-FTIR analysis. When voltage is applied, the propellant undergoes an electrolytic reaction where the ions of the oxidizing salt are transported to the electrodes, where they undergo an exothermic oxidation-reduction reaction. A variety of propellants were sampled, consisting of both AP and LP co-oxidizers, and various fuel wt%. A binary mixture of AP and PEG was the primary propellant utilized in further analysis due to its favorable ignition characteristics and consistent propagation. The propellant was manufactured through a solution casting technique. However, thermogravimetric analysis indicated that after formulation, no residual solvent was retained in the propellant. This is an important result, as much of the previous work with electrically controlled propellants relied on residual solvent to enhance conduction, and the lack of solvent results in a higher performing propellant with better aging characteristics. Ignition experiments were carried out with two primary electrode configurations: 1) parallel, and 2) concentric. Within each primary configuration, several variations were explored. In the majority of experiments, ignition occurred at the anode, where the perchlorate ion is oxidized. In the case of parallel electrodes, increasing the length and thereby surface area of the electrodes decreases ignition delay, which can be attributed to an increase in available reaction sites. In addition, ignition delay decreased linearly with increasing voltage when electrodes of the same length were used. Additional experiments were conducted with uneven electrodes, meaning one electrode was longer than the other. The effect of this is to restrict the process at the smaller electrode. Thus, with a long anode, reduction is limited, while with a long cathode, oxidation is limited. When oxidation was limited, it resulted in very long ignition delays at low voltages, which decreased quickly with increasing voltage. When reduction was limited, ignition delays first increased with increasing voltage before decreasing again at the highest voltage. Interestingly, this was also the only condition in which ignition did not exclusively occur at the anode. This behavior is indicative of a mechanism change. Current and temperature data suggest an increasing resistance and enhanced Joule heating near the cathode with increasing voltage when reduction was limited. This can be attributed to the enhanced formation of gases/bubbles along the cathode, increasing the apparent bulk resistance of the propellant, resulting in a shift from an electrochemically driven ignition to a thermally enhanced ignition. The concentric electrode configuration experiments generally demonstrated consistent behavior with the parallel electrode ignition experiments. That is, when oxidation or reduction was limited, the overall behavior was similar to that of the parallel electrode configurations. The lone exception to this was that initial decomposition occurred near the inner electrode, regardless of polarity, due to the higher field strength in this region. In the case of the parallel electrodes, initial decomposition always occurred at the cathode via a well-established PEG instability. However, the temperature profiles preceding ignition still indicated a dependence on the rate-limiting redox half reaction due to the electrode surface area. This is particularly prominent in the cases of limited reduction, which result in increased bulk resistivity and shifting the ignition mechanism from electrochemical to thermal.

6.2 Future Work

While this work has contributed to understanding the mechanisms of electrically initiated polymer electrolyte propellants, several critical areas remain insufficiently explored. In particular, the role of pressure on ignition behavior and subsequent combustion dynamics remains poorly understood. Elevated pressures are known to enhance thermal feedback, potentially influencing ignition delay times, reaction zone structure, and flame propagation regimes. A systematic study of pressure-dependent behavior, incorporating both experimental and modeling approaches, is necessary to elucidate the coupled thermal, electrical, and chemical feedback mechanisms at play.

Moreover, although this study provides new insights into ignition phenomena, the complex rheological behavior of polymer electrolyte matrices provides further research in understanding pre-ignition and transient combustion species transport. Further work is required to decouple the effects of viscosity, ionic conductivity, and polymer microstructure on ignition threshold and stability. This could involve parametric studies across a broader range of formulations and the use of polymer electrolyte surrogate models to better characterize reactive transport.

Additionally, the interfacial phenomena governing energy deposition at the electrode-propellant boundary remain an area of limited resolution. Detailed characterization of local electric field distributions, Joule heating, and electrochemical reaction kinetics at ignition-relevant timescales may reveal new pathways for optimizing ignition efficiency and repeatability. Advanced diagnostics such as microscale thermometry and in situ spectroscopy could be deployed to resolve these transient processes with higher fidelity.

From a theoretical standpoint, the development of multiphysics models that capture the interplay between electrical conduction, thermal diffusion, and chemical kinetics in spatially inhomogeneous systems would significantly enhance predictive capabilities. These models should account for the influence of dynamic material properties, phase transitions, and localized instabilities.

Finally, while practical applications are beyond the immediate scope of this work, future studies may consider how these fundamental insights can inform the design of energetically favorable formulations or structured energetic media. However, the primary focus should remain on refining the scientific understanding of the ignition and combustion processes in these complex, coupled systems.

Bibliography

[1] G.P Sutton and O. Biblarz. Rocket propulsion elements. pages Chaps. 1,7,13,19. John Wiley and Sons, 9th ed. edition, 2017.

[2] Philip Hill and Carl Peterson. Mechanics and thermodynamics of propulsion. In *Mechanics of Thermodynamics of Propulsion*. Pearson, 2 edition, 1992. ISBN 0-201-14659-2.

[3] Philip D. Umholtz. The history of solid rocket propulsion and aerojet, April 1999. URL `https://apps.dtic.mil/sti/pdfs/ADA406104.pdf`.

[4] Luigi T. DeLuca. *Chemical Rocket Propulsion: A Comprehensive Survey of Energetic Materials*, pages 1015–1032. Springer International Publishing, 2017. ISBN 978-3-319-27748-6. doi: 10.1007/978-3-319-27748-6_42.

[5] Ernest Sutton. *From polymers to propellants to rockets - A history of Thiokol.* doi: 10.2514/6.1999-2929.

[6] J. Hunley. *The history of solid-propellant rocketry - What we do and do not know.* doi: 10.2514/6.1999-2925.

[7] John D. Clark. *Ignition! An Informal History of Liquid Rocket Propellants.* Rutgers University Press, 1972. ISBN 0-8135-0725-1.

[8] Milton Lehman and Charles A. Lindbergh. *This high man : the life of Robert H. Goddard.* Farrar, Straus, New York, 1963. Section: xv, 430 pages illustrations, portraits 22 cm.

[9] Hermann Oberth. *The Rocket into Planetary Space*. De Gruyter Oldenbourg, Berlin, München, Boston, 2014. ISBN 9783110367560. doi: doi:10.1515/9783110367560. URL https://doi.org/10.1515/9783110367560.

[10] Eric Boyer and Kenneth Kuo. *Characteristics of Nitromethane for Propulsion Applications*. doi: 10.2514/6.2006-361.

[11] Chaturvedi Shalini and Dave Pragnesh N. Solid propellants: Ap/htpb composite propellants. *Arabian Journal of Chemistry*, 2019. doi: 10.1016/j.arabjc.2014.12.033.

[12] D.D Evans and T.W Price. The status of monopropellant hydrazine technology, February 1968.

[13] Bradley Gobin, Nicholas Harvey, Charles Arnold, Sean Whalen, and Greg Young. Utilization of ionically conducting polymers in electrically controlled gel monopropellants. In *AIAA SCITECH 2022 Forum*. 2021. doi: 10.2514/6.2022-2361.

[14] Manisha B. Padwal, Benveniste Natan, and D.P. Mishra. Gel propellants. *Progress in Energy and Combustion Science*, 83, 2021. https://doi.org/10.1016/j.pecs.2020.100885.

[15] GAD NACHMONI and BENVENISTE NATAN. Combustion characteristics of gel fuels. *Combustion Science and Technology*, 1999. https://doi.org/10.1080/00102200008947300.

[16] Manisha B. Padwal, Benveniste Natan, and D. P. Mishra. Gel propellants. *Progress in Energy and Combustion Science*, 83:100885, March 2021. doi: 10.1016/j.pecs.2020.100885.

[17] Qingfei Fu, Fei Ge, Wenda Wang, and Lijun Yang. Spray characteristics of gel propellants in an open-end swirl injector. *Fuel*, 254:115555, October 2019. ISSN 0016-2361. doi: 10.1016/j.fuel.2019.05.138.

[18] D. E. Daney and A. S. Rapial. Preparation and characterization of slush hydrogen and nitrogen gels. In K. D. Timmerhaus, editor, *Advances in Cryogenic Engineering*, pages 467–475, Boston, MA, 1995. Springer US. ISBN 978-1-4757-0513-3.

[19] Olwen Morgan and Dennis Meinhardt. *Monopropellant selection criteria - Hydrazine and other options.* doi: 10.2514/6.1999-2595.

[20] William M. Marshall and Matthew C. Deans. *Recommended Figures of Merit for Green Monopropellants.* doi: 10.2514/6.2013-3722.

[21] Fiona Leverone, Angelo Cervone, and Eberhard Gill. Cost analysis of solar thermal propulsion systems for microsatellite applications. *Acta Astronautica*, 155, 11 2018. doi: 10.1016/j.actaastro.2018.11.025.

[22] Eugene F. Rothgery. *Hydrazine and Its Derivatives.* John Wiley Sons, Ltd, 2004. ISBN 9780471238966. doi: https://doi.org/10.1002/0471238961.0825041819030809.a01.pub2.

[23] Anders Larsson and Niklas Wingborg. Green propellants based on ammonium dinitramide (adn). In Jason Hall, editor, *Advances in Spacecraft Technologies*, chapter 7. IntechOpen, Rijeka, 2011. doi: 10.5772/13640.

[24] Tommy W Hawkins, Adam Brand, Milton McKay, and Michael Tinnirello. Reduced toxicity, high performance monopropellant at the u.s. air force research laboratory. 2010. URL `https://api.semanticscholar.org/CorpusID:39062695`.

[25] Anders Larsson and Niklas Wingborg. Green propellants based on ammonium dinitramide (adn). In Jason Hall, editor, *Advances in Spacecraft Technologies*, chapter 7. IntechOpen, Rijeka, 2011. doi: 10.5772/13640.

[26] Dominic Freudenmann and Helmut K. Ciezki. Adn and han-based monopropellants – a minireview on compatibility and chemical stability in aqueous media. *Propellants, Explosives, Pyrotechnics*, 44(9):1084–1089, 2019. doi: https://doi.org/10.1002/prep.201900127.

[27] Robert Wilson. Dinitramide salts: Adn plus other salts. Technical report, SRI International, 2012. URL `https://web.archive.org/web/20120526005446/http://www.sri.com/psd/research/adn.html`.

[28] Dennis Meinhardt, Gerry Brewster, Stacy Christofferson, and E. Wucherer. *Development and testing of new, HAN-based monopropellants in small rocket thrusters.* doi: 10.2514/6.1998-4006.

[29] Robert L. Sackheim and Robert K. Masse. Green propulsion advancement: Challenging the maturity of monopropellant hydrazine. *Journal of Propulsion and Power*, 30 (2):265–276, 2014. doi: 10.2514/1.B35086.

[30] Robert Jankovsky. *HAN-based monopropellant assessment for spacecraft.* doi: 10.2514/6.1996-2863.

[31] Robert Masse, May Allen, Ronald Spores, and Elizabeth A. Driscoll. *AF-M315E Propulsion System Advances and Improvements.* doi: 10.2514/6.2016-4577.

[32] Ronald A. Spores. *GPIM AF-M315E Propulsion System.* doi: 10.2514/6.2015-3753.

[33] Keiichi Hori, Toshiyuki Katsumi, Shujiro Sawai, Nobuyuki Azuma, Keigo Hatai, and Junichi Nakatsuka. Han-based green propellant, shp163 – its r&d and test in space. *Propellants, Explosives, Pyrotechnics*, 44(9):1080–1083, 2019. doi: https://doi.org/10.1002/prep.201900237.

[34] Corentin Maleix, Pierre Chabernaud, Rachid Brahmi, Romain Beauchet, Yann Batonneau, Charles Kappenstein, Martin Schwentenwein, Robert-Jan Koopmans, Sebastian Schuh, and Carsten Scharlemann. Development of catalytic materials for decomposition of adn-based monopropellants. *Acta Astronautica*, 158:407–415, 2019. ISSN 0094-5765. doi: https://doi.org/10.1016/j.actaastro.2019.03.033.

[35] Rachid Amrousse, Toshiyuki Katsumi, Yosui Niboshi, Nobuyuki Azuma, Ahmed Bachar, and Keiichi Hori. Performance and deactivation of ir-based catalyst during hydroxylammonium nitrate catalytic decomposition. *Applied Catalysis A: General*, 452:64–68, 2013. ISSN 0926-860X. doi: https://doi.org/10.1016/j.apcata.2012.11.038.

[36] Ahmed E. S. Nosseir, Angelo Cervone, and Angelo Pasini. Review of state-of-the-art green monopropellants: For propulsion systems analysts and designers. *Aerospace*, 8 (1), 2021. ISSN 2226-4310. doi: 10.3390/aerospace8010020.

[37] Edgar Choueiri. *A Critical History of Electric Propulsion: The First Fifty Years (1906-1956)*. doi: 10.2514/6.2004-3334.

[38] Grant Risha, Richard A. Yetter, and Vigor Yang. Electrolytic-induced decomposition and ignition of han-based liquid monopropellants. *International Journal of Energetic Materials and Chemical Propulsion*, 6(5):575–588, 2007. ISSN 2150-766X.

[39] D. C. Sayles. Development of test motors for advanced controllable propellants. *Journal of Spacecraft and Rockets*, 12(3):174–178, 1975. doi: 10.2514/3.56962.

[40] D. C. Sayles and C. T. Levinsky. Advanced pintle-controlled motor with thrust vector control. *SAE Transactions*, 80:2557–2564, 1971. ISSN 0096736X, 25771531. URL http://www.jstor.org/stable/44650341.

[41] Bhavik A. Patel. Chapter 1 - introduction to electrochemistry for bioanalysis. In

Bhavik Patel, editor, *Electrochemistry for Bioanalysis*, pages 1–8. Elsevier, 2020. ISBN 978-0-12-821203-5.

[42] J. Koryta, J. Dvorak, and L. Kavan. *Principles of Electrochemistry*. Wiley, 1993. ISBN 9780471938385.

[43] John O'M. Bockris and Amulya K.N. Reddy. *Modern Electrochemistry 1: Ionics*. Plenum Press, 1998. ISBN 0306455552.

[44] Margaret Robson Wright. *An Introduction to Aqueous Electrolyte Solutions*. Wiley, 2007. ISBN 978-0-470-84293.

[45] P. J. Mayo, L. A. Watermeier, and F. J. Weinberg. Electrical control of solid propellant burning. *Proceedings of the Royal Society of London. Series A, Mathematical and Physical Sciences*, 284(1399):488–498, 1965. ISSN 00804630. URL `http://www.jstor.org/stable/2415152`.

[46] R. BESTGEN and H. WRIGHT. *A study of the effects of electric fields on solid propellant burningrates*. doi: 10.2514/6.1971-174.

[47] Gregory Young, Jeremy J. Koeck, Nathaniel T. Conlin, Jordan L. Sell, and Grant A. Risha. Influence of an electric field on the burning behavior of solid fuels and propellants. *Propellants, Explosives, Pyrotechnics*, 37(1):122–130, 2012. doi: https://doi.org/10.1002/prep.201100052.

[48] Walter L. Petty. Variation in shell 405 catalyst physical characteristics, test catalyst preparation. *SHELL DEVELOPMENT CO HOUSTON TX*, 1973. https://apps.dtic.mil/sti/tr/pdf/AD0769888.pdf.

[49] Stanley E. Wood and James T. Bryant. Decomposition of hydrazine on shell 405 catalyst at high presure. *Product R&D*, 12(2):117–122, 1973. doi: 10.1021/i360046a004.

[50] Eckart Schmidt and E. Wucherer. Hydrazine(s) vs. nontoxic propellants – where do we stand now? *European Space Agency, (Special Publication) ESA SP*, 10 2004.

[51] Rachid Amrousse, Keiichi Hori, Wafa Fetimi, and Kamal Farhat. Corrigendum to: "han and adn as liquid ionic monopropellants: Thermal and catalytic decomposition processes" [appl. catal. b: Environ. 127 (2012) 121–128]. *Applied Catalysis B: Environmental*, 158-159:426–428, 2014. ISSN 0926-3373. doi: https://doi.org/10.1016/j.apcatb.2014.03.050.

[52] Donald G. Harlow, Rowland E. Felt, Steve Agnew, G. Scott Barney, J. Malvyn McKibben, Robert Garber, and Margie Lewis. Technical report on hydroxylamine nitrate. Technical report, USDOE Office of Environment, Health, Safety and Security (AU); USDOE Office of Nuclear Safety Basis Facility Design, 02 1998.

[53] Rachid Amrousse, Toshiyuki Katsumi, Nobuyuki Azuma, and Keiichi Hori. Hydroxylammonium nitrate (han)-based green propellant as alternative energy resource for potential hydrazine substitution: From lab scale to pilot plant scale-up. *Combustion and Flame*, 176:334–348, 2017. ISSN 0010-2180. doi: https://doi.org/10.1016/j.combustflame.2016.11.011.

[54] Wai Siong Chai, Kean How Cheah, Ming-Hsun Wu, Kai Seng Koh, Dashan Sun, and Hua Meng. A review on hydroxylammonium nitrate (han) decomposition techniques for propulsion application. *Acta Astronautica*, 196:194–214, 2022. ISSN 0094-5765. doi: https://doi.org/10.1016/j.actaastro.2022.04.011.

[55] Michele Negri and Marius Wilhelm. New technologies for ammonium dinitramide based monopropellant thrusters - the project rheform. *Acta Astronautica*, 143:105–117, 2018. ISSN 0094-5765. doi: https://doi.org/10.1016/j.actaastro.2017.11.016.

[56] Laurence Courthéoux, Dan Amariei, Sylvie Rossignol, and Charles Kappenstein. Thermal and catalytic decomposition of hnf and han liquid ionic as propellants. *Applied Catalysis B: Environmental*, 62(3):217–225, 2006. ISSN 0926-3373. doi: https://doi.org/10.1016/j.apcatb.2005.07.016.

[57] Michele Negri. Replacement of hydrazine: Overview and first results of the h2020 project rheform. *6TH EUROPEAN CONFERENCE FOR AERONAUTICS AND SPACE SCIENCES (EUCASS)*, 2015. doi: https://elib.dlr.de/100693/1/Negri_2015_EUCASS.pdf.

[58] Marius Wilhelm, Michele Negri, Helmut Ciezki, and Stefan Schlechtriem. Preliminary tests on thermal ignition of adn-based liquid monopropellants. *Acta Astronautica*, 158: 388–396, 2019. ISSN 0094-5765. doi: https://doi.org/10.1016/j.actaastro.2018.05.057.

[59] Prashant Khare, Vigor Yang, Hua Meng, Grant A. Risha, and Richard A. Yetter. Thermal and electrolytic decomposition and ignition of han–water solutions. *Combustion Science and Technology*, 187(7):1065–1078, 2015. doi: 10.1080/00102202.2014.993033.

[60] G. Klingenberg, H.J. Frieske, and H. Rockstroh. Electrical ignition of han-based liquid propellants. Technical report, Fraunhofer-Institut fUr Kurzzeit- dynamik, Ernst-Mach-Institut (EMI-AFB, 1990. https://apps.dtic.mil/sti/tr/pdf/ADA223272.pdf.

[61] R. Yetter, V. Yang, Z. Wang, Y. Wang, I. Aksay, F. Dryer, J. Pelluse, D. Milius, and M. Angioletti. *Development of Meso and Micro Scale Liquid Propellant Thrusters*. doi: 10.2514/6.2003-676.

[62] Ming-Hsun Wu and Richard A. Yetter. A novel electrolytic ignition monopropellant microthruster based on low temperature co-fired ceramic tape technology. *Lab Chip*, 9:910–916, 2009. doi: 10.1039/B812737A.

[63] Wai Siong Chai, Dashan Sun, Kean How Cheah, Gang Li, and Hua Meng. Co-electrolysis-assisted decomposition of hydroxylammonium nitrate–fuel mixtures using stainless steel–platinum electrodes. *ACS Omega*, 5(31):19525–19532, 2020. doi: 10.1021/acsomega.0c01804. PMID: 32803046.

[64] Kilsu Park and Taegyu Kim. Experimental studies on effects of electrode material and voltage on electrolytic decomposition of hydroxylammonium nitrate solution. *Acta Astronautica*, 216:267–274, 2024. ISSN 0094-5765. doi: https://doi.org/10.1016/j.actaastro.2024.01.008.

[65] Wai Siong Chai, Kean How Cheah, Hua Meng, and Gang Li. Experimental and analytical study on electrolytic decomposition of han-water solution using graphite electrodes. *Journal of Molecular Liquids*, 293:111496, 2019. ISSN 0167-7322. doi: https://doi.org/10.1016/j.molliq.2019.111496.

[66] Hao Huang, Miranda Trentle, Zexin Liu, Kehui Xiang, William Higgins, Yunbing Wang, Bing Xue, and Shuguang Yang. Polymer complex fiber: Property, functionality, and applications. *ACS Applied Materials & Interfaces*, 15(6):7639–7662, February 2023. ISSN 1944-8244. doi: 10.1021/acsami.2c19583. Publisher: American Chemical Society.

[67] Daniel T. Hallinan and Nitash P. Balsara. Polymer electrolytes. *Annual Review of Materials Research*, 43:503–525, 2013. ISSN 1545-4118. doi: https://doi.org/10.1146/annurev-matsci-071312-121705.

[68] Shujahadeen B. Aziz, Thompson J. Woo, M.F.Z. Kadir, and Hameed M. Ahmed. A conceptual review on polymer electrolytes and ion transport models. *Journal of Science: Advanced Materials and Devices*, 3(1):1–17, 2018. ISSN 2468-2179. doi: https://doi.org/10.1016/j.jsamd.2018.01.002.

[69] Zhigang Xue, Dan He, and Xiaolin Xie. Poly(ethylene oxide)-based electrolytes for lithium-ion batteries. *J. Mater. Chem. A*, 3(38):19218–19253, 2015. doi: 10.1039/C5TA03471J. Publisher: The Royal Society of Chemistry.

[70] Hongwei Zhang and Pei Kang Shen. Recent development of polymer electrolyte membranes for fuel cells. *Chemical Reviews*, 112(5), 2012. doi: 10.1021/cr200035s.

[71] G. Hirankumar and N. Mehta. Effect of incorporation of different plasticizers on structural and ion transport properties of pva-liclo4 based electrolytes. *Heliyon*, 4(12), 2018. ISSN 2405-8440. doi: https://doi.org/10.1016/j.heliyon.2018.e00992.

[72] Lizhen Long, Shuanjin Wang, Min Xiao, and Yuezhong Meng. Polymer electrolytes for lithium polymer batteries. *J. Mater. Chem. A*, 4, 2016. doi: 10.1039/C6TA02621D.

[73] Zlatka Gadjourova, Yuri G. Andreev, David P. Tunstall, and Peter G. Bruce. Ionic conductivity in crystalline polymer electrolytes. *Nature*, 412(6846):520–523, aug 2001. doi: 10.1038/35087538.

[74] Anders Hagfeldt, Gerrit Boschloo, Licheng Sun, Lars Kloo, and Henrik Pettersson. Dye-sensitized solar cells. *Chemical Reviews*, 110(11), 2010. doi: 10.1021/cr900356p.

[75] Masayoshi WATANABE, Satoshi NAGANO, Kohei SANUI, and Naoya OGATA. Ionic conductivity of network polymers from poly(ethylene oxide) containing lithium perchlorate. *Polymer Journal*, 18, 1986. https://doi.org/10.1295/polymj.18.809.

[76] Florian Gebert, Jonathan Knott, Robert Gorkin, Shu-Lei Chou, and Shi-Xue Dou. Polymer electrolytes for sodium-ion batteries. *Energy Storage Materials*, 36:10–30, 2021. ISSN 2405-8297. doi: https://doi.org/10.1016/j.ensm.2020.11.030.

[77] Ming Zhu, Jiaxin Wu, Yue Wang, Mingming Song, Lei Long, Sajid Hussain Siyal, Xiaoping Yang, and Gang Sui. Recent advances in gel polymer electrolyte for high-

performance lithium batteries. *Journal of Energy Chemistry*, 37:126–142, 2019. ISSN 2095-4956. doi: https://doi.org/10.1016/j.jechem.2018.12.013.

[78] Wayne N Sawka and Michael McPherson. Electrical solid propellants: A safe, micro to macro propulsion technology. In *49th AIAA/ASME/SAE/ASEE Joint Propulsion Conference*, 2013. https://arc.aiaa.org/doi/abs/10.2514/6.2013-4168.

[79] Wayne N. Sawka, Arthur Katzakian, and Charles Grix. Solid state digital propulsion ”cluster thrusters” for small satellites using high performance electrically controlled extinguishable solid propellants (ecesp). Technical report, Marshall Space Flight Center, 2005. https://ntrs.nasa.gov/api/citations/20050223573/downloads/20050223573.pdf.

[80] Andrew Hiatt and Robert A. Frederick. Laboratory experimentation and basic research investigating electric solid propellant electrolytic characteristics. doi: 10.2514/6.2016-4935.

[81] Lirong Bao, Wei Zhang, Xiaojun Zhang, Yongyi Chen, Suhang Chen, Lizhi Wu, Ruiqi Shen, and Yinghua Ye. Impact of mwcnt/al on the combustion behavior of hydroxyl ammonium nitrate (han)-based electrically controlled solid propellant. *Combustion and Flame*, 2020. https://doi.org/10.1016/j.combustflame.2020.05.013.

[82] Lirong Bao, Hui Wang, Zhiwen Wang, Haiming Xie, Shujie Xiang, Wei Zhang, Yinsheng Huang, Ruiqi Shen, and Yinghua Ye. Controllable ignition, combustion and extinguishment characteristics of han-based solid propellant stimulated by electric energy. *Combustion and Flame*, 2022. https://doi.org/10.1016/j.combustflame.2021.111804.

[83] Lirong Bao, Hui Wang, Tingting Zheng, Suhang Chen, Wei Zhang, Xiaojun Zhang, Yinsheng Huang, Ruiqi Shen, and Yinghua Ye. Exploring the influences of conduc-

tive graphite on hydroxylammonium nitrate (han)-based electrically controlled solid propellant. *Propellants, Explosives, Pyrotechnics*, 2020. DOI: 10.1002/prep.202000049.

[84] Sean Whalen, Emily Sellards, Bradley Gobin, and Gregory Young. Exploring the influence of additives on the ignition, combustion and quenching of electrically controlled solid propellants. *Propellants, Explosives, Pyrotechnics*, 49(6), 2024. doi: https://doi.org/10.1002/prep.202300299.

[85] Zhicheng He, Zhixun Xia, Jianxin Hu, and Yang Li. Lithium-perchlorate/polyvinyl-alcohol-based aluminized solid propellants with adjustable burning rate. *Journal of Propulsion and Power*, 35(3):512–519, 2019. doi: 10.2514/1.B37279.

[86] Yang Li, Zhi xun Xia, Jian xin Hu, Li kun Ma, Xu dong Na, and Zhi cheng He. Experimental investigation of the ignition and combustion characteristics of electrically controlled solid propellant. *Acta Astronautica*, 184:167–179, 2021. ISSN 0094-5765. doi: https://doi.org/10.1016/j.actaastro.2021.04.012.

[87] George G. Marvin and Lawrence B. Woolaver. Thermal decomposition of perchlorates. *Industrial & Engineering Chemistry Analytical Edition*, 17(8):474–476, 1945. doi: 10.1021/i560144a004.

[88] Bradley Gobin, Nicholas Harvey, and Gregory Young. Influence of polymer electrolytes on electrically controlled energetic materials. *AIAA SCITECH*, 2022. https://doi-org.ezproxy.lib.vt.edu/10.2514/6.2022-2362.

[89] Bradley Gobin, Sean Whalen, Emily M. Plunkett, Garratt F. Godshall, Robert B. Moore, and Gregory Young. Effect of electrical stimuli on combustion behavior of solid oxidizers. *International Journal of Energetic Materials and Chemical Propulsion*, 2021. 10.1615/IntJEnergeticMaterialsChemProp.2021038286.

[90] Inna Zamir, Dan Grinstein, and Alon Gany. Testing electric effects on the burning rate of ammonium-nitrate-based solid propellants. *International Journal of Energetic Materials and Chemical Propulsion*, 16(1):39–47, 2017. ISSN 2150-766X.

[91] Inna Zamir, Moshe Ben-Reuven, Alon Gany, and Dan Grinstein. Investigation of electrically controlled ammonium nitrate – epoxy solid propellant at high pressures. *Propellants, Explosives, Pyrotechnics*, 46(3):477–483, 2021. doi: https://doi.org/10.1002/prep.202000208.

[92] Kanagaraj Gnanaprakash, Daehong Lim, and Jack J. Yoh. Combustion characteristics of lithium perchlorate-based electrically controlled solid propellants at elevated pressures. *Thermochimica Acta*, 720, 2023. https://doi.org/10.1016/j.tca.2022.179421.

[93] Kanagaraj Gnanaprakash, Meng Yang, and Jack J. Yoh. Thermal decomposition behaviour and chemical kinetics of tungsten based electrically controlled solid propellants. *Combustion and Flame*, 238, 2022. https://doi.org/10.1016/j.combustflame.2021.111752.

[94] Yang Li, Zhi-xun Xia, Li-kun Ma, and Xu-dong Na. Ignition and extinction characteristics of electrically controlled solid propellants. *Journal of Propulsion and Power*, 39(3):340–350, 2023. doi: 10.2514/1.B38807.

[95] Saima Sultana and Rafiuddin. Behaviour of electrical conductivity in csi–al2o3 and csi–tio2 systems. *Arabian Journal of Chemistry*, 9, 2016. ISSN 1878-5352. doi: https://doi.org/10.1016/j.arabjc.2011.02.025.

[96] Michel Armand and Gustaaf Van Tendeloo. Solid polymer electrolytes-fundamentals and technological applications. *Advanced Materials*, 4(10):691–692, 1992. doi: https://doi.org/10.1002/adma.19920041022.

[97] Emily Sellards. Comparison of cation-anion oxidizer pairings in electrically controllable solid propellants. Master's thesis, Virginia Polytechnic Institute and State University, 2024.

[98] A.F.J. Goeting and J.A.A. Ketelaar. The mechanism of the nitrate (platinum) electrode in molten alkali nitrates. *Electrochimica Acta*, 19(6):267–271, 1974. ISSN 0013-4686. doi: https://doi.org/10.1016/0013-4686(74)85077-2.

[99] Udo Anders and James A. Plambeck. Electrochemistry of fused lithium perchlorate. *Journal of The Electrochemical Society*, 115(6):598, jun 1968. doi: 10.1149/1.2411355.

[100] Benveniste Natan and Dov Hasan. Advances in gel propulsion. *International Journal of Energetic Materials and Chemical Propulsion*, 18(4):303–323, 2019. ISSN 2150-766X.

[101] H. Ciezki, Karl Naumann, and Volker Weiser. Status of gel propulsion in the year 2010 with a special view on the german activities. 01 2010.

[102] K. Hodge, T. Crofoot, and S. Nelson. *Gelled propellants for tactical missile applications.* doi: 10.2514/6.1999-2976.

[103] Botchu Vara Siva Jyoti, Muhammad S. Naseem, Seung Wook Baek, Hyung Ju Lee, and Sung June Cho. Hypergolicity and ignition delay study of gelled ethanolamine fuel. *Combustion and Flame*, 183:102–112, 2017. ISSN 0010-2180. doi: https://doi.org/10.1016/j.combustflame.2017.05.007.

[104] Shai Rahimi and Benveniste Natan. The status of gel propellants in year 2000. *International Journal of Energetic Materials and Chemical Propulsion*, 5(1-6):172–194, 2002. ISSN 2150-766X.

[105] GAD NACHMONI and BENVENISTE NATAN. Combustion characteristics of gel

fuels. *Combustion Science and Technology*, 156(1):139–157, 2000. doi: 10.1080/00102200008947300.

[106] Richard Arnold and William Anderson. *Droplet Burning of JP-8/Silica Gels.* doi: 10.2514/6.2010-421.

[107] Qinliu Cao, Wenhe Liao, Wei-Tao Wu, and Feng Feng. Combustion characteristics of inorganic kerosene gel droplet with fumed silica as gellant. *Experimental Thermal and Fluid Science*, 103:377–384, 2019. ISSN 0894-1777. doi: https://doi.org/10.1016/j.expthermflusci.2019.01.031.

[108] C. K. Law. Mechanisms of droplet combustion. *JPL Proc. of the 2d Intern. Colloq. on Drops and Bubbles*, March 1, 1982. https://ntrs.nasa.gov/api/citations/19820015551/downloads/19820015551.pdf.

[109] S. Gordon and B.J McBride. Computer program for calculation of complex chemical equilibrium compositions and applications. Technical report, NASA Rept. RP-1311, 1994.

[110] N. Kubota. *Propellants and Explosives: Thermochemical Aspects of Combustion*, pages 71–72. Wiley VCH, 2016.

[111] V.V. Boldyrev a. Thermal decomposition of ammonium perchlorate. *Thermochimica Acta*, 443, 2006. https://doi.org/10.1016/j.tca.2005.11.038.

[112] M.C. Hegg and A.V. Mamishev. Influence of variable plate separation on fringing electric fields in parallel-plate capacitors. In *Conference Record of the 2004 IEEE International Symposium on Electrical Insulation*, pages 384–387, 2004. doi: 10.1109/ELINSL.2004.1380606.

[113] M Chase. *NIST-JANAF Thermochemical Tables, 4th Edition.* American Institute of Physics, -1, 1998-08-01 1998.

[114] Yan Kou, Siyu Wang, Jipeng Luo, Keyan Sun, Jian Zhang, and Zhicheng Tan andQuan Shi. Thermal analysis and heat capacity study of polyethylene glycol (peg) phase change materials for thermal energy storage applications. *The Journal of Chemical Thermodynamics*, 2018.

[115] Harrison Autry, Bradley Gobin, Ryan Marks, Gregory Young, Afrida Anis, Prithwish Biswas, Keren Shi, Yujie Wang, and Michael R. Zachariah. Impact of ammonium perchlorate content on electrically controlled gel polymer electrolyte monopropellants. *Journal of Propulsion and Power*, 40(4):612–620, 2024. doi: 10.2514/1.B39250.

[116] Bradley Gobin, Paul Reiter, Sean Whalen, and Gregory Young. Extinguishing and combustion characteristics of electrically controllable solid propellants under elevated pressures. *Journal of Propulsion and Power*, 40(1):152–163, 2024. doi: 10.2514/1.B39189.

[117] M. J. M. Bernal and H. S. W. Massey. Metallic ammonium. , 114:172, January 1954. doi: 10.1093/mnras/114.2.172.

[118] Tae Young Kim, Seunghoe Choe, and Jae Jeong Kim. Decomposition of polyethylene glycol (peg) at cu cathode and insoluble anode during cu electrodeposition. *Electrochimica Acta*, 357:136803, 2020. ISSN 0013-4686. doi: https://doi.org/10.1016/j.electacta.2020.136803.

[119] Jonathon R. Harding, Chibueze V. Amanchukwu, Paula T. Hammond, and Yang Shao-Horn. Instability of poly(ethylene oxide) upon oxidation in lithium–air batteries. *The Journal of Physical Chemistry C*, 119(13):6947–6955, 2015. doi: 10.1021/jp511794g.

[120] Afrida Anis, Keren Shi, Erik Hagen, Yujie Wang, Prithwish Biswas, and Michael R. Zachariah. Role of anions in the electrochemical modulation of flammability of ionic liquids. *Combustion and Flame*, 275, 2025. ISSN 0010-2180. doi: https://doi.org/10.1016/j.combustflame.2025.113994.